2014-09-23

Nitric Oxide Chemistry and Velocity Slip Effects in Hypersonic Boundary Layers

Arisman, Christopher

UNIVERSITY OF CALGARY

Nitric Oxide Chemistry and Velocity Slip Effects in Hypersonic Boundary Layers

by

Christopher J. Arisman

A THESIS

SUBMITTED TO THE FACULTY OF GRADUATE STUDIES

IN PARTIAL FULFILMENT OF THE REQUIREMENTS FOR THE

DEGREE OF MASTER OF SCIENCE

DEPARTMENT OF MECHANICAL AND MANUFACTURING ENGINEERING

CALGARY, ALBERTA

SEPTEMBER, 2014

Abstract

Simulations of gas seeding into a hypersonic boundary layer flow were performed using OpenFOAM to investigate and quantify errors associated with quantitative planar laser induced fluorescence thermometry and velocimetry techniques. A modified version of the compressible rhoCentralFoam solver was used to simulate multicomponent chemically reactive flows. Simulations replicated conditions used in NASA Langley's 31" Mach 10 facility with a wedge model oriented at various angles of attack. The magnitude and location of potential reactions were estimated through the use of an analytical half-life model and non-reactive simulations. These estimates were compared to the reactive simulations. The order of magnitude predictions were found to be accurate when a simulated estimate of the distribution of nitric oxide was used. The effect of the heat release due to chemical reactions on the velocity and temperature profiles was investigated and found to be negligible for all positive angles of attack.

Preface

This thesis includes research that has been conducted in collaboration with a number of individuals. Sections of Chapter 3 were revised and edited by P. Danehy who also contributed to the previous work performed in ANSYS Fluent by C. Johansen. The experimental data presented in Chapter 3 was processed by B. Bathel. Comparisons between the numerical results obtained by the author of this thesis and the experimental data were also performed and written in part by Bathel. In addition to the experimental data the chapter was revised and edited by Bathel.

Chapter 3 and 5 include works that have been presented at the 43rd Fluid Dynamics Conference in San Diego. The full citation reads:

Arisman, C., Johansen, C. T., Galuppo, W., & McPhail, A. Nitric Oxide Chemistry Effects in Hypersonic Boundary Layers. In 43rd Fluid Dynamics Conference. San Diego, CA: American Institute of Aeronautics and Astronautics. doi:10.2514/6.2013-3104

The primary authors of this article were the author of this thesis and Johansen. W. Galuppo and A. McPhail contributed preliminary coding work to the development of the solver used in the research. Johansen supervised the research as well as revised and edited the publication.

Acknowledgements

I would like to thank Miss Charlotte Jones whose motivational speech consisting of "why not?" finally convinced me to undertake this degree. I would also like to thank my supervisor, Dr. Craig Johansen, for giving me this opportunity and sharing with me his knowledge and experience. Dr. Brett Bathel and Dr. Paul Danehy, thank you for your criticism, insight, and contributions to this research. To my fellow students and co-workers, thank you for putting up with me for the last two years; I hope you have learned as much from me as I did from you. Finally I would like to thank my mother for removing all (most) of the superfluous commas from this thesis.

Table of Contents

List of Tables

List of Figures and Illustrations

List of Symbols, Abbreviations and Nomenclature

Abbreviations

AoA	Angle of Attack
Br_2	Molecular Bromine
CFD	Computational Fluid Dynamics
CFI	Computational Fluid Imaging
Cl_2	Molecular Chlorine
CLBL	Compressible Laminar Boundary Layer
DGV	Doppler Global Velocimetry
DNS	Direct Numerical Simulation
ENO	Essentially Non-Oscillatory
I_2	Molecular Iodine
Kr	Krypton
LIF	Laser Induced Fluorescence
MTV	Molecular Tagging Velocimetry
MW	Molecular Weight
N_2	Molecular Nitrogen
N_2O_4	Dinitrogen Tetroxide
NO	Nitric Oxide
NO_2	Nitrogen Dioxide
NO_3	Nitrogen Trioxide
NO_x	Mono-nitrogen Oxide
O_2	Molecular Oxygen

OH	Hydroxyl Radical
PIV	Particle Image Velocimetry
PLIF	Planar Laser Induced Fluorescence
PPM	Peicewise Parabolic Method
RCS	Reaction Control System
RKDG	Runge-Kutta Discontinuous Galerkin
sccm	Standard Cubic Centimeters per Minute
SCRAMJET	Supersonic Combustion ramjet
TPS	Thermal Protection Shield
WENO	Weighted Essentially Non-Oscillatory

Latin Symbols

A	Arrhenius reaction rate constant
B	Arrhenius reaction rate constant
C	Arrhenius reaction rate constant
c_p	Specific heat at constant pressure
d_c	Characteristic length
$D_{i,j}$	Binary diffusion coefficient
$D_{i,m}$	Diffusion coefficient of species i into the mixture
$d_{s,i}$	Average collision diameter of seed gas s and bulk gas i
E_a	Arrhenius reaction rate activation energy
h_i	Sensible enthalpy of species i
h_s	Sensible enthalpy

I	Identity matrix
J_i	Diffusion flux of species i
K	Thermal conductivity
Kn	Knudsen number
k_{NO}	Reaction rate of NO
$L_{1/2}$	Half-life length scale
L_d	Computational domain length
L_{sim}	Local simulation length scale
Ma	Mach number
m_i	Molecular mass of species i
M_i	Molar mass of species i
m_s	Molecular mass of seed gas
$\dot{m}_s$	Mass flow rate of seed gas
n_{ideal}	Ideal molar concentration
n_{sim}	Simulated molar concentration
P	Pressure
P_{inf}	Freestream pressure
P_{stag}	Stagnation pressure
R	Ideal gas constant
Re	Reynolds number
R_i	Mass source of species i
r_{le}	Wedge leading edge radius
S_h	Enthalpy source

t	Time
T	Temperature
$t_{1/2}$	Half-life
T_{stag}	Stagnation Temperature
U	Velocity
u_o	Flow velocity
u_{inf}	Freestream velocity
u_{slip}	Slip velocity
u_x	Velocity in x direction
W_z	Wedge width
x_{slot}	Length of seed slot
Y_i	Mass fraction of species i

Greek Symbols

α	Thermal conductivity divided by specific heat at constant pressure
β	Oblique shock angle
δ	Boundary layer thickness
Δ	Mesh cell thickness
θ_{plate}	Plate angle of attack
λ	Mean free path
μ	Viscosity
ρ	Density
$\sigma_{i,j}$	Average species collision diameter

σ_u	Maxwell slip model accommodation coefficient
τ	Viscous stress tensor
τ_{St}	Particle relaxation time
X_{NO}	Mol fraction of NO
$X_{NO,i}$	Initial mol fraction of NO
X_{O_2}	Mol fraction of O2
$X_{O_2,i}$	Initial mol fraction of O2
Ω_d	Diffusion collision integral
Ω_v	Viscous collision integral

Chapter 1: Introduction

1.1 Background and Motivation

1.1.1 Transition-to-turbulence

In the wake of the Columbia space shuttle disaster, a major recommendation from the Columbia Accident Investigation Board was the development of computational tools that could determine the risks involved during re-entry as a result of damage to a flight vehicle's thermal protection systems (TPS) (Cockrell, Barnes, Belvin, Allmen, & Otero, 2005). Damage to a vehicle's TPS could be sustained during launch or while in orbit. Because repair of the TPS would likely require a spacewalk, the risks of the spacewalk need to be weighed against the risk of attempting re-entry with a damaged TPS. An integral part of these computational tools is the accurate prediction of the transition-to-turbulence. The transition-to-turbulence process in a hypersonic boundary layer and subsequent breakdown to turbulence can result in significantly increased heat transfer rates to a flight vehicle's surface. Increased heat transfer rates pose a significant risk to the vehicle's TPS, the vehicle and its payload (Horvath et al., 2006).

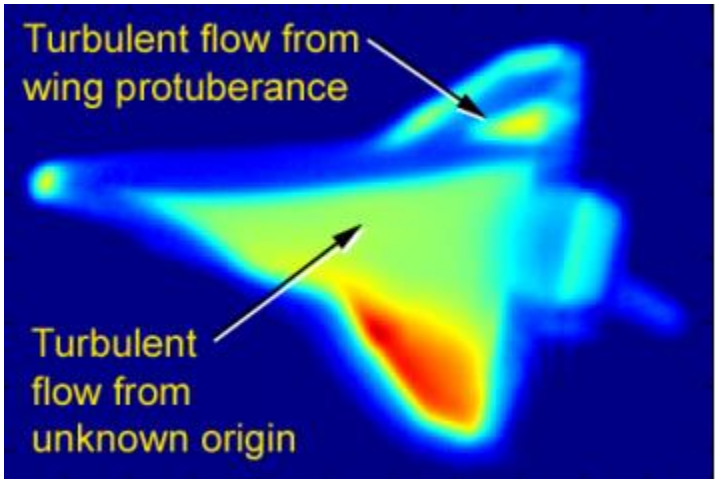

Figure 1.1: Surface temperature distribution during discovery re-entry flight experiment. Reproduced from Horvath et al., (2010)

Figure 1.1 shows an infrared image taken from a flight experiment conducted on the Discovery space shuttle during re-entry (Horvath et al., 2010). Prior to the shuttle's launch a tile with a protuberance was placed in a non-critical spot on the vehicle's TPS. The protuberance was designed to cause an early transition-to-turbulence in the boundary layer. This was done in an effort to obtain data that could be used to improve computational modelling capabilities. Shown in the figure is the increased temperature on the surface of the shuttle's TPS as a result of early turbulence transition. While the pre-flight prediction of when the boundary layer would become turbulent was quite good (within one standard deviation) the predicted peak temperature was off by over a factor of four. Also of interest in the figure is the turbulent flow from an unknown origin where transition-to-turbulence also occurred unexpectedly early. These differences between the experimental and predicted temperature highlight the need for better predictive methods that are able to more accurately predict the heat loads on flight vehicle TPS.

Predictive methods can be improved by gaining better insight into the physical mechanisms governing the transition-to-turbulence and turbulent heat transfer processes. These

methods could also be used to better select and size a TPS, ensuring the flight vehicle is adequately insulated while avoiding excess insulation and more importantly weight that is associated with uncertainties in current predictive capabilities. As vehicle design tools rely on computational fluid dynamics (CFD), relevant experimental data is critical for numerical model validation. Since hypersonic boundary layer stability can be very sensitive to flow disturbances, non-intrusive techniques are often preferred when collecting experimental data.

1.1.2 Hypersonic Boundary Layer Seeding

The tracking of a tracer species is a common non-intrusive method to facilitate flow visualization and to obtain quantitative measurements of flow variables. The tracer follows the flow and can then be imaged, revealing flow structures for further analysis. Tracers vary between techniques; techniques like planar laser-induced fluorescence (PLIF) use a gas species capable of fluorescence excitation that has the ability to follow the flow field and can provide quantitative velocity, temperature and concentration measurements in addition to flow visualization. In some experimental setups the tracer species occurs naturally in the flow. A good example of this is in combustion flows where the hydroxyl radical, OH, is present. In high-enthalpy facilities that use air as the test gas, tracer species such as nitric oxide (NO) form at high temperatures and can be uniformly distributed when flowed into the test section. However, in many situations a seed gas is required. Examples of when seeding is required for PLIF flow visualization include the study of fuel-air mixing for supersonic combustion ramjet (SCRAMJET) engines (Fox et al., 2001) and the study of reaction control system jet interactions with hypersonic crossflows associated with planetary entry vehicles (B. Bathel, Danehy, Inman, Alderfer, & Berry, 2008; P. M. Danehy et al., 2009; J. A. Inman, Danehy, Alderfer, Buck, & McCrea, 2009).

When seeding a fluorescent species into a flow there are a number of things to consider. The seeding strategy should make sure not to alter the flow features of interest. For example, hypersonic boundary layer stability can be very sensitive, and has the potential to be altered by small flow disturbances such as surface defects on the test model. As a result, hypersonic boundary layer studies are particularly concerned with the way the seeding strategy alters boundary layer stability. Important flow parameters like Mach number, Reynolds number or Prandlt number can also be altered by the seed gas.

NO is a common seed gas used to facilitate PLIF data collection in hypersonic flows. NO is often preferred when the bulk flow medium is air as its thermophysical properties and molecular size are close to that of the species present in air; reducing adverse effects of seeding (C. Johansen & Danehy, 2012). However, the seeding of NO introduces other potential adverse effects that need to be quantified. NO reacts with O_2 in air at low temperatures in a termolecular, exothermic, reaction (Olbregts, 1985). This reaction is of particular concern in hypersonic wind tunnels that use NO PLIF as a flow visualization technique because the flow temperatures are often quite low due to the large expansion required to achieve high Mach numbers. The NASA Langley Research Center's 31-inch Mach 10 Air Tunnel is an example of such a facility that produces low temperature freestream conditions where NO chemistry could be a problem. There have been several experiments in that facility where NO PLIF was used to study the transition-to-turbulence (B. Bathel et al., 2010; P. Danehy, Ivey, Bathel, et al., 2010; P. Danehy, Ivey, Inman, et al., 2010; Medford et al., 2011).

1.2 **Hypersonic Wind Tunnel Facility and Experiments**

Figure 1.2 shows a schematic of the NASA Langley Research Center's 31-inch Mach 10 wind tunnel facility. Seen in the figure is the test section; the viewing section is shown on the left hand side of the figure with the camera setup. The laser system can be seen on the right of the facility.

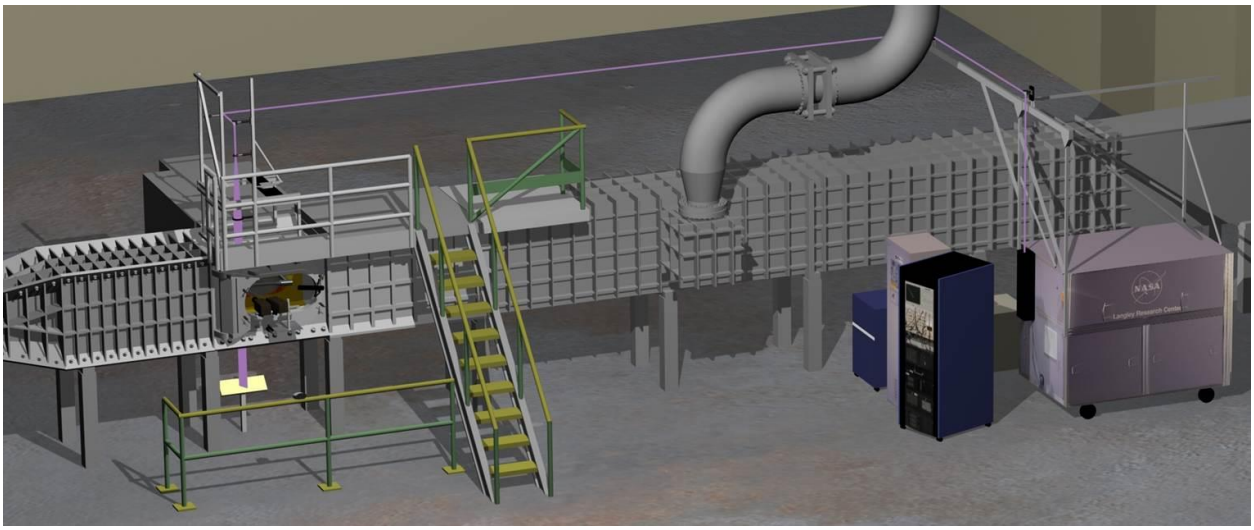

Figure 1.2: NASA Langley 31" Mach 10 Air Tunnel Facility with PLIF systems. Reproduced from Medford et al. (2011)

In the NASA Langley PLIF experiments, a planar, 20 degree wedge with a sharp leading edge (r_{le} = 0.024±0.005 mm) was placed into the test section and NO gas was seeded through a slot on the model to allow for PLIF images to be obtained downstream. A series of protuberance shapes with various heights were mounted on the wedge surface; PLIF flow visualization and quantitative molecular tagging velocimetry (MTV) measurements were obtained. Figure 1.3 shows the wedge model, gas seeding slot, pressure tap, and a cylindrical trip that was used during several of the experiments (P. Danehy, Ivey, Inman, et al., 2010). The figure also contains an overlay of a sample PLIF image taken during one of the experimental runs. The PLIF image shows a region of laminar flow prior to the cylindrical trip. After the flow encounters the

cylindrical trip it becomes unstable and transitions to turbulence, which can be seen on the downstream side of the wedge.

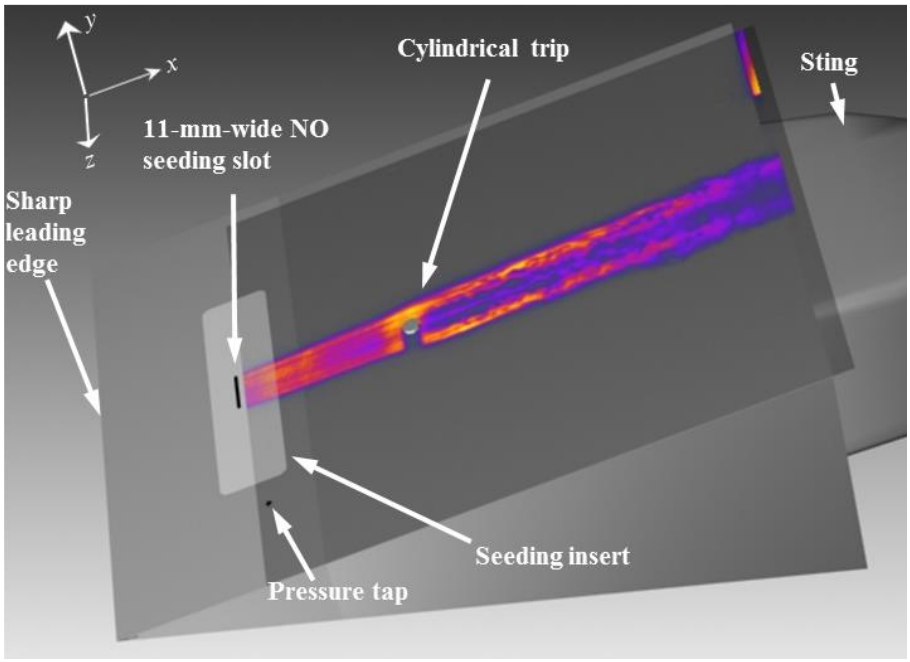

Figure 1.3: Schematic of wedge model, indicating the gas seeding slot and a cylindrical-shaped trip. Reproduced from P. Danehy, Ivey, Inman, et al., (2010)

Table 1.1 Experimental wind tunnel model details.

Model Parameter	Attribute
Model surface material	Stainless steel
Model surface ($L_x \times W_z$)	162.5-mm × 127.5-mm
Seeding slot ($L_x \times W_z$)	0.8-mm × 11.0-mm
Location of seeding slot center x_{slot}	29.4-mm
Leading edge radius, r_{le}	0.024±0.005 mm
Plate angles (θ)	5°,1°
Stagnation Pressure (psi)	150 - 1450

Table 1 provides a summary of the attributes of the model used in the NO PLIF experiments and in the simulations presented in this paper. Details of the 31-Inch Mach 10 Air Blowdown facility used in the NO PLIF experiments are provided in Micol (1998). In this facility, the

stagnation pressure and model angle of attack (AoA) can be varied to produce different post-shock edge conditions, including Reynolds number, on the wedge surface.

1.3 **Research Objectives**

The need to quantify negative effects associated with the gas seeding process into a hypersonic boundary layer motivated a numerical study comparing several typical PLIF seed gases injected from the wedge model (C. Johansen & Danehy, 2012). The gases simulated included NO, Krypton (Kr), and Iodine (I_2). Although Kr and I_2 are non-reactive with oxygen (O_2), they have a much higher molecular weight (MW) than NO and air resulting in large differences in their respective thermophysical properties. For a given mass flow rate of seeded gas it was found that NO had the largest dispersion rate and penetrated the furthest into the boundary layer, which is desired for the transition-to-turbulence experiments. Measurements far from the wall are desired because transition to turbulence has been shown to begin near the edge of the boundary layer in hypersonic flows (Fischer, 1972). Also of interest is the boundary layer edge velocity, which is often inferred from oblique shock calculations but may not be accurate due to viscous interaction effects (Anderson, 2000).

In addition to boundary layer penetration the seeding of NO had the smallest adverse effect on velocity and temperature profiles downstream. The study did not investigate the effects of model AoA or any possible chemistry effects of NO on the boundary layer profiles. Therefore the focus of the current study is to investigate these effects. A methodology of assessing the chemistry effects analytically is also presented.

The study also did not consider any potential velocity slip at the wall due to rarefied effects. While the freestream Knudsen number based on plate length was approximately Kn = 0.003, the Knudsen number at the wall based on boundary layer thickness varies such that rarefied effects

may be significant near the leading edge where the boundary layer thickness is relatively small and the Knudsen number relatively large (>0.01). As a result the impact of slip at the wall on the simulation results will also be assessed.

Chapter 2: Literature Review

The work being investigated involves a seed gas being injected into a hypersonic cross flow. This is accomplished through the use of a slotted jet oriented normal to the wedge surface. As a result, previous work done on gasses injected from both jets and slots into hypersonic cross flows are of interest.

2.1 Jet in Hypersonic Cross Flow

There are a number of studies investigating circular jets in supersonic cross flows. Investigations into this type of flow are of particular interest due to the complex 3D flow structures generated in the vicinity of the jet (Chan & Roger, 1993; Fric & Roshko, 1994; Gruber, Nejadt, Chen, & Dutton, 1995). A detailed schematic of these flow structures is shown in Figure 2.1. Figure 2.1 was reproduced from Dickmann & Lu, (2006) and is based on the research performed by Champigny & Lacau, (1994). Of note in the figure are the horseshoe vortices that form when the approaching boundary layer wraps around the cross flow jet, the bow shock from the flow deflection, the lambda shock from the shockwave-boundary layer interaction between the bow shock and boundary layer, and the barrel shock formed by the jet plume which ends with a Mach disk.

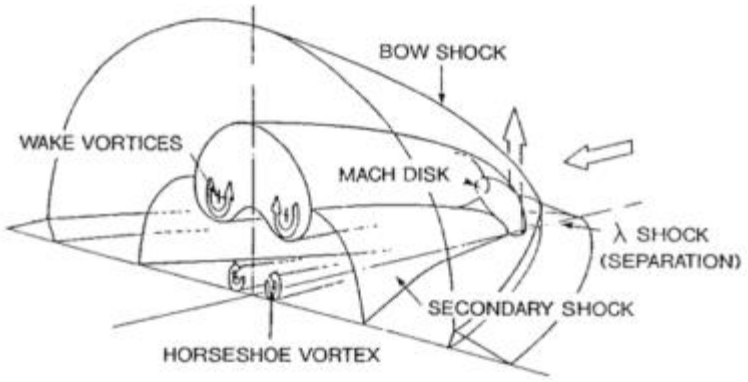

Figure 2.1: Jet in supersonic cross flow 3D flow structures; reproduced from Champigny & Lacau, (1994); Dickmann & Lu, (2006)

In addition to the interesting flow structures, reaction control systems (RCS) often rely on jets positioned on the body of a flight vehicle to provide attitude control (Champigny & Lacau, 1994). Srinivasan & Bowersox (2004) investigated the impact of the barrel shock that forms in the cross flow and its influence on the resulting flow field. The shock/boundary layer interaction in the vicinity of the cross flow jet has been investigated by Dickmann & Lu (2009) for both subsonic and supersonic cross flows.

Strip blowing occurs when the cross flow jet is a rectangular strip with the length direction oriented perpendicular to the flow. This configuration changes the inherently 3D problem of the jet in cross flow to something that can be approximated by a 2D model when the region of interest is far enough away from the edges of the strip. A detailed schematic of the 2D flow can be seen in Figure 2.2 and was reproduced from Messiter & Matarrese, (1995).

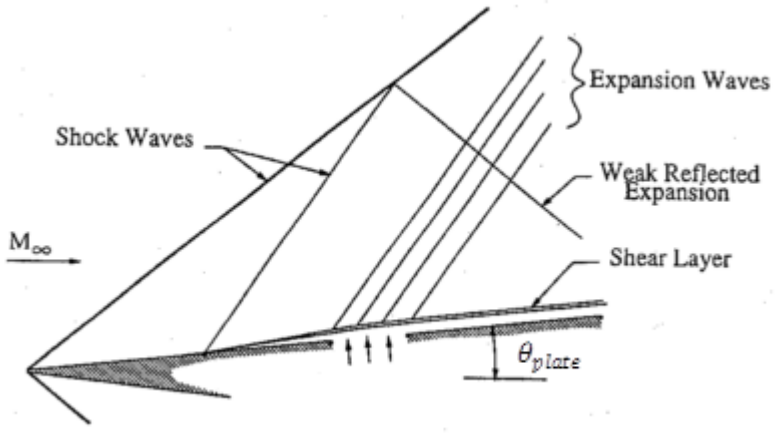

Figure 2.2: Wedge flow with strip blowing; reproduced from Messiter & Matarrese, (1995)

Some of the earliest work on strip blowing was performed by Smith & Stewartson (1973). In this work expressions for the wall pressure and boundary-layer thickness were derived for a flat plate in a supersonic flow with strip injection of a gas. The work assumed that the flow was laminar and that jet flow was strong enough to cause separation upstream of the slot but not

strong enough to blow the boundary layer off the wall. This work was extended to wedges at hypersonic speeds by Messiter & Matarrese (1995). In both the aforementioned works weak viscous interaction was assumed.

The expressions for surface pressure were further expanded by Matarrese, Messiter, & Adamson (1991) to account for both weak and strong viscous interaction. The work assumed strong blowing where the boundary layer is blown away from the wedge surface as a free shear layer. The expressions were also derived to allow for an arbitrary seed gas.

Numerical investigations into strip blowing have primarily been focused on boundary layer stability with instabilities introduced by oscillations in the cross flow exiting the strip. Ghaffari, Marxen, Iaccarino, & Shaqfeh (2010) performed Navier-Stokes simulations as well as linear stability analysis of a hypersonic flat plate flow with boundary-layer wall strip blowing. Direct numerical simulations (DNS) of strip blowing into a Mach 20 free stream were performed by Stemmer (2002) to investigate boundary layer transition-to-turbulence. In this work the disturbance source was again from the strip at the wall. Also of interest is a study performed by Ankudinov (1972) who numerically investigated the blowing of a foreign gas into the shock layer of a hypersonic flow. This work was for a spherical blunt body.

2.2 **CFD Solver and Numerical Scheme**

The solver used in this work is a modified version of the density based OpenFOAM solver known as rhoCentralFoam. The rhoCentralFoam central-upwind scheme was developed by Kurganov, Noelle, & Petrova, (2001) and is based on the work by Nessyahu & Tadmor, (1990). It is semi-discrete and non-staggered, such that it can operate with collocated meshes as developed by Kurganov & Tadmor, (2000). This type of scheme was developed since solution

variables, such as velocity and pressure, are often collocated in popular CFD software packages, including OpenFOAM.

The advantage of the central-upwind scheme over other schemes in the OpenFOAM toolkit is that it can produce non-oscillatory solutions near flow discontinuities. Examples of other numerical schemes that can accurately treat flow discontinuities include the monotone upstream-centered schemes for conservation laws (van Leer, 1997), piecewise parabolic method (PPM) (Colella & Woodward, 1984), essentially non-oscillatory (ENO) schemes (Harten, Engquist, Osher, & Chakravarthy, 1987), weighted ENO (WENO) schemes (Liu, Osher, & Chan, 1994), and the Runge-Kutta discontinuous Galerkin (RKDG) method (Cockburn & Shu, 1998). None of these schemes are included in the standard OpenFOAM package.

A detailed description of rhoCentralFoam can be found in Greenshields et al. (2010) where rhoCentralFoam has been used to solve supersonic flow over a forward facing step, supersonic jet, and shock tube. The rhoCentralFoam solver in its standard form does not include the capability to simulate species transport or include chemical reactions. A modified version has been used to solve radiation associated with hypersonic flows around re-entry vehicles (Bansal, Feldick, & Modest, 2012). A similar compressible OpenFOAM solver developed by Chapuis *et al*. has been used to simulate supersonic combustion and gaseous explosions (Chapuis, Fureby, Fedina, Alin, & Tegnér, 2010).

2.3 **NO Chemistry**

The chemistry of NO is of particular interest to a broad variety of fields. NO can react with a number of molecules to form NO_2 in a termolecular reaction. These molecules include O_2 as well as molecular chlorine (Cl_2) and bromine (Br_2) (Hisatsune & Zafonte, 1969). Due to this any study involving NO must also have a good understanding of NO_2 formation to fully assess and

account for the effects of any potential reactions. In combustion processes these reactions are of interest as NO and its reaction products (NO_x) become atmospheric pollutants when the exhaust gasses are vented. As a result there is a wide variety of data available for the reaction at high temperatures (Ashmore, Burnett, & Tyler, 1962; Morecroft & Thomas, 1967) for NO_2 and NO_x formation in combustion processes. Data is also available for the reaction at room temperature and parts per million concentrations (Glasson & Tuesday, 1963; Greig & Hall, 1966, 1967) for atmospheric pollution studies.

In this work the reaction of NO with O_2 to form NO_2 is of interest. The reaction rate constant has been found to be independent of pressure and partial pressure of reactants (Hisatsune & Zafonte, 1969). It has also been found to be independent of the presence of nitrogen (Hisatsune & Zafonte, 1969). Various experiments have fit the reaction rate to a temperature dependent Arrhenius rate. A summary of experimentally determined reaction rates and their respective ranges of validity can be found in Tsukahara, Ishida, & Mayumi (1999). Because the free stream temperature in this study is quite low (~52 K), lower temperature reaction rates are of particular importance. The lowest temperature reaction rate was determined by Olbregts (1985) and is valid for a temperature range of 226 K to 758 K.

In his work Olbregts noted that the reaction rate increased as temperature decreased below 600 K. Olbregts brought up two well-known multi-step mechanisms in an attempt to explain this inverse temperature dependence:

$$NO + O_2 \rightarrow NO_3 \tag{2.1}$$

$$NO_3 \rightarrow NO + O_2 \tag{2.2}$$

$$NO_3 + NO \rightarrow 2NO_2 \tag{2.3}$$

and

$$2NO \rightarrow (NO)_2 \quad (2.4)$$

$$(NO)_2 \rightarrow 2NO \quad (2.5)$$

$$(NO)_2 + O_2 \rightarrow 2NO_2 \quad (2.6)$$

Olbregts hypothesized, based on the fact that both NO_3 and $(NO)_2$ have been observed in experiments (Laane & Ohlsen, 1980), that both of the mechanisms are both present in the flow and competing such that one is dominant above 600 K and has a positive temperature dependence and vice versa for the other.

2.4 **Flow Visualization Techniques**

There are a number of techniques that can be used to visualize flow structures in hypersonic flows. Some common methods include schlieren photography, particle image velocimetry (PIV), Doppler global velocimetry (DGV) and PLIF.

Schlieren photography is a method that visualizes changes in the refractive index of a fluid. In the context of supersonic flows, the working principal behind schlieren photography is that density gradients in the flow cause variations in the refractive index (Settles, 2012). When a light source is combined with a number of optics, the variations in the refractive index can be captured and used to identify flow structures. Schlieren photography is particularly useful for identifying shock structures in supersonic flows (Bogdonoff, 2012). However, because the method is based on density gradients, it is not suitable for studies where the gradients are small or the density is low (J. Inman, 2007). In the case of the work described here, the density gradients and the overall density in the boundary layer is relatively small. This would not result in a high quality schlieren image in the region of interest.

PIV involves tracking tracer particles seeded in the flow. Two images are taken in quick succession and then cross-correlated to estimate the velocity field of the particles. If the particles

are the correct size and have sufficiently low mass their velocity field will accurately represent that of the flow. The ability of a particle to accurately track the flow is characterized by the Stokes number:

$$\mathrm{St_k} = \frac{\tau_{St} * U_o}{d_c} \tag{2.7}$$

where U_o is the flow velocity, d_c is the characteristic length of the flow and τ_{St} is the relaxation time of the particles. τ_{St} measures the particle's tendency to reach velocity equilibrium with the carrier fluid and is proportional to the particle density and diameter. A low (<0.1) stokes number corresponds to particles accurately tracking the flow (Tropea, Yarin, & Foss, 2007).

In some cases, the particles may not accurately track the flow. In particular there are often particle tracking issues in regions where the velocity gradient is large (Gharib, 1997). The addition of particles in the boundary layer may also alter the transition-to-turbulence within the boundary layer. This is of particular concern as one of the main goals of the experiments was improving the prediction and modeling of turbulence in hypersonic boundary layer flows. Additionally, the particles need to be relatively distinguishable. This is an issue in hypersonic flows as the particles may need to be quite small in order to accurately track the flow. More rigorous details on the PIV technique can be found in Raffel, Willert, Wereley, & Kompenhans, (2007).

DGV measures the Doppler shift in the frequency of light scattered by particles in the flow (McKenzie, 1996). The measured Doppler shift can then be used to determine the velocity field and image the flow. Unlike PIV, the particles used in DGV do not need to be distinguishable from each other. As a result smoke could be used to seed the flow, which would overcome the flow tracking issues in the presence of large velocity gradients. However, DGV does not provide

a good signal-to-noise ratio in regions of low density where there may be insufficient amounts of smoke present (Schwartz, 2001). As a result it is likely not suitable for the types of hypersonic boundary layer studies performed as low pressure and density conditions are present. Additionally the smoke may not penetrate to the edge of the velocity boundary layer in sufficient quantities.

The PLIF technique used in the experiments mentioned in this study is an of application laser induced fluorescence (LIF) in two dimensions. In its simplest form LIF involves the excitation of a molecule through the absorption of a photon from a laser. The excited molecule, now at a higher energy state, can transition back to its original lower energy state through two methods. It can either collide with an adjacent molecule in what is known as collisional quenching or fluoresce and return back to its lower energy state by emitting a photon. The emitted photon is then captured by a camera. A more detailed description of the LIF technique with a focus on NO and OH LIF in combustion processes can be found in Battles & Hanson, (1995).

In the case of Planar LIF (PLIF), optics are used to stretch the laser into a sheet, expanding the visualization area to a two dimensional plane in the flow. The PLIF technique has been used in a wide variety of experiments. Some experiments of note include the imaging of supersonic turbulent combustion in a scramjet combustor (C. T. Johansen et al., 2014) and the modelling of heat shield ablation using naphthalene (Combs, Clemens, & Danehy, 2014).

Chapter 3: OpenFOAM Solver Development and Validation

3.1 Governing Equations

The standard rhoCentralFoam solver has been modified to create the rhoCentralReactingFoam solver used in this work. Compared to the other Navier Stokes solvers available in the OpenFOAM toolkit, rhoCentralFoam includes the dissipation function in the energy equation, which is required to predict viscous heating near wall boundaries. The solver also accurately captures flow discontinuities (e.g. shock waves) through the use of a central-upwind finite volume discretization scheme (Greenshields et al., 2010).

In its standard form, rhoCentralFoam solves the unsteady, compressible Navier-Stokes equations for single species laminar and turbulent flows. Whereas the standard rhoCentralFoam solver computes the transport of total energy, the modified version solves the sensible enthalpy equation (Eq. (3.3)) in order to easily include the chemical reaction and species transport terms from the reactingFoam solver (Afarin, Tabejamaat, & Mardani, 2011). The conservation of mass, momentum (neglecting body forces), and energy used by the rhoCentralReactingFoam solver are defined as:

$$\frac{\partial \rho}{\partial t} + \nabla \cdot (\rho u) = 0 \tag{3.1}$$

$$\frac{\partial (\rho u)}{\partial t} + \nabla \cdot (\rho u^2) = -\nabla P + \nabla \cdot \tau \tag{3.2}$$

$$\frac{\partial (\rho h_s)}{\partial t} + \nabla \cdot (\rho u h_s) - \frac{DP}{Dt} = \nabla \cdot [\alpha \nabla h_s + \sum_{i=1}^{n} h_i J_i] + \nabla \cdot (\tau \cdot u) + S_h \tag{3.3}$$

where ρ , u, P, h_s, T, S_h are the gas density, velocity, pressure, sensible enthalpy, temperature and enthalpy source respectively. α is defined as $\frac{k}{c_p}$ where k is the thermal conductivity and c_p is the specific heat at constant pressure. The viscous stress tensor, τ, in vector form is defined as:

$$\tau = \mu(\nabla u + (\nabla u)^T - \frac{2}{3}\nabla \cdot uI) \tag{3.4}$$

where μ is the viscosity and I is the unit tensor. The viscous stress tensor is 2μ multiplied by the deviatoric component of the deformation gradient tensor.

The enthalpy transport term, $\sum_{i=1}^{n} h_i J_i$, has been included in the energy equation, which allows for variable Prandtl, Schmidt, and Lewis numbers. In the standard reactingFoam solver, these variables are treated as a constant with the Lewis number assumed to be equal to one. The thermal conductivity is calculated from a modified Euken correction equation taken from the work of Hollis (Hollis, 1996):

$$k = \mu\left(\frac{15}{4} - 1.32\left(\frac{c_p}{R} - \frac{5}{2}\right)\right)R \tag{3.5}$$

Specific heat values for NO, I_2 and Kr were taken from the NIST-JANAF tables (National Institute of Standards and Technology, 2011). The viscosity is calculated based on kinetic theory from the Chapman-Cowling relationship also found in the work of Hollis (Hollis, 1996):

$$\mu = 2.6693 * 10^6 \frac{\sqrt{MT}}{\sigma\Omega_v} \tag{3.6}$$

Because the rhoCentralFoam solver is limited to single species non-reacting flows in its standard form, modifications were implemented to expand its capability and solve hypersonic flows with multispecies gas mixtures. In order to use it to investigate gas seeding, species transport and diffusion coefficient modeling were added. Implementation of these features in

rhoCentralReactingFoam is based on the structure of the available solver, reactingFoam (Afarin et al., 2011). The transport of multiple species mass fraction (Y_i) for both solvers, neglecting thermal diffusion, is given by the following conservation equation:

$$\frac{\partial(\rho Y_i)}{\partial t} + \nabla \cdot (\rho u Y_i) = -\nabla \cdot J_i + R_i \tag{3.7}$$

where J_i is the diffusion flux of species *i* and is defined as:

$$J_i = -\rho D_{i,m} \nabla Y_i \tag{3.8}$$

The standard reactingFOAM solver assumes a unity Schmidt number in the species conservation equation. Since a variable Schmidt number is required for the current simulation, a binary species diffusion coefficient has been included in the species conservation equation. For both solvers the binary diffusion coefficient, $D_{i,m}$, for species *i* in the mixture is given by Wilke's equation (Wilke, 1950):

$$\mathrm{D_{i,m}} = \frac{1 - X_i}{\sum_{j,j \neq i}^{n} \frac{X_j}{D_{i,j}}} \tag{3.9}$$

where X_i is the molar fraction of species *i* and $D_{i,j}$ is the binary diffusion coefficient which was calculated using the Chapman-Enskog equation (Brodkey & Hershey, 2003):

$$D_{i,j} = 0.00188 \frac{\left[T^3 \left(\frac{1}{M_a} + \frac{1}{M_b}\right)\right]^{\frac{1}{2}}}{P \sigma_{ab}^2 \Omega_d} \tag{3.10}$$

where σ_{ab} is the average species collision diameter based on tabulated values published by Svehla (Svehla, 1962) and Ω_d is the diffusion collision integral (Neufeld, Janzen, & Aziz, 2003). For the diffusion coefficient calculation *P* is in bar. M_a and M_b are the molecular weights of species a and b respectively. All mixture properties are calculated based on a mass weighted average of the individual species properties.

The rhoCentralReactingFoam solver handles viscous effects by first solving the inviscid equation and using the inviscid solution as a predictor for the viscous solution, correcting for the diffusive terms (Greenshields et al., 2010). The solver is unsteady and steady state solutions are obtained by marching forward in time until fluctuations in flow variables no longer subsist (Greenshields et al., 2010). Since the Reynolds number of the flow, based on the freestream velocity and plate length, is small ($Re = 3.4\times10^5$), turbulence modeling is not required in the simulations. However, rhoCentralFoam does have the ability to use built-in Reynolds Averaged Navier Stokes (RANS) and Large Eddy Simulation (LES) turbulence models for higher Reynolds number flows.

3.2 **Simulation Setup**

The computational domain is based on the wedge model used in the experiments performed in NASA Langley's 31-inch Mach 10 facility (Medford et al., 2011). A schematic of the computational domain relative to the wedge model and sting is shown in Figure 3.1. The domain is two dimensional, 200 mm in length (*x* direction) and 30 mm in height (*y* direction). The origin of the coordinate system is at the leading edge of the wedge. The gas is seeded from a slot that is 0.81 mm wide and 11 mm deep located 29.4 mm downstream of the leading edge. An inlet section for the seed gas equal to four seed slot widths in length was included in the computational domain.

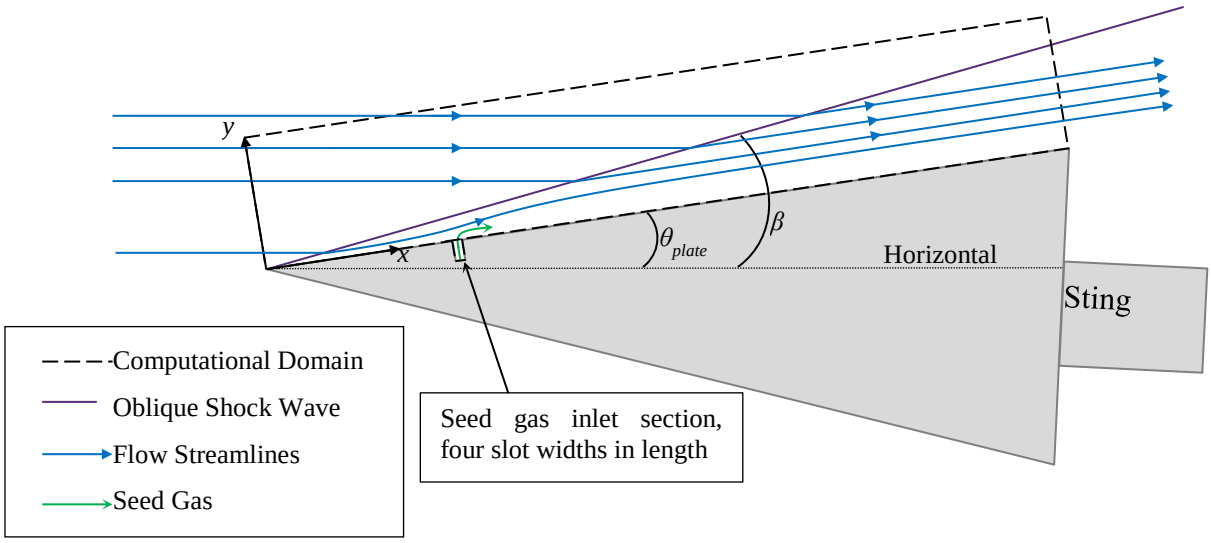

Figure 3.1: Computational domain

The bottom of the domain is aligned with the top surface of the wedge. Changes in plate angle (θ_{plate}) are controlled by specifying the inlet velocity (direction) on the top and left boundaries. Constant pressure, temperature, and velocity values of P = 68.4 Pa, T = 52.3 K, and u = 1407.3 m/s (Ma = 9.7) are specified at the inlet boundaries which correspond to one of the experimental run conditions. These freestream values were calculated from the facility stagnation pressure (P_{stag} = 350 psi, 2.41 MPa) and temperature (T_{stag} = 1000 K) values specified in one of the representative tests. Equations relating the stagnation conditions to the freestream values are outlined in the literature (Hollis, 1996). In the simulations, the wedge was oriented at an angle of θ_{plate} = 5° and 1°. The bottom wall is specified as a no-slip condition, zero normal gradient in pressure and fixed temperature (T = 314 K). The fixed temperature was determined from the experimental data at this condition. The right outflow boundary is specified as zero normal gradient for the temperature, velocity and pressure boundary conditions.

The walls of the seed gas inlet section were modeled as slip boundaries and given a constant static temperature of 314 K. The total temperature of the pipe inflow boundary was calculated based on the desired mass flow rate and the pressure at the jet outlet. Two sets of simulations were performed; one with the seed slot closed and one with the seed gas on. For the seeding simulations seed gas mass flow rate, $\dot{m}_s$, was equal to 3 mg/s, which is equivalent to 150 standard cubic centimeters per minute (sccm). This is typical for NO PLIF in NASA Langley Research Center's 31-inch Mach 10 Air Tunnel facility.

The finite volume schemes used were as follows:

- Flux scheme: Kurganov
- Time stepping scheme: Euler
- Gradient scheme: Gauss linear
- Divergence scheme: Gauss linear
- Interpolation scheme: Gamma 1.0

Finite volume schemes are named based on their OpenFOAM toolkit conventions. Any options not mentioned here were based on the available rhoCentralFoam wedge tutorial. Chemistry options were based on the reactingFOAM counter flow flame tutorial.

3.3 **Mesh Sensitivity Results**

Figure 3.2 shows resulting rhoCentralReactingFoam mesh which consists of approximately 1.2 million nodes. The grid is refined near the leading edge, at the gas injection slot and near the bottom wall. The cells are then graded, increasing in size as the domain moves away from the seed slot and the bottom wall. Further refinement beyond the 1.2 million nodes had a negligible impact on the simulation results.

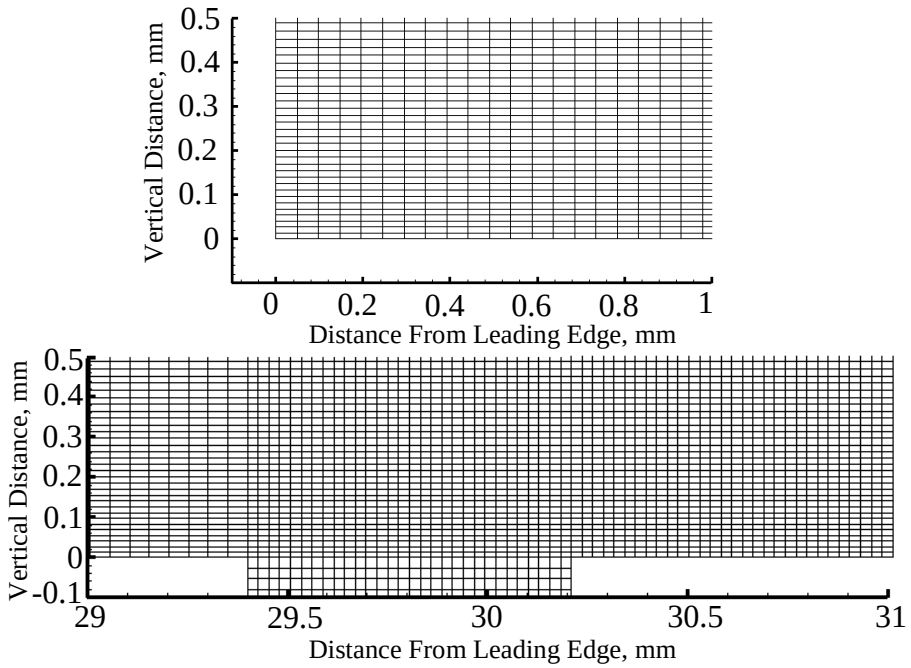

Figure 3.2: Computational grid near leading edge (top) and at gas seeding location (bottom).

Figure 3.3 shows the effect of grid cell spacing on distributions of temperature for the rhoCentralReactingFoam solver; Δ is the cell size and is taken at the center of the boundary layer. Initial simulations using the rhoCentralReactingFoam solver used a Δ = 0.1 mm in the vertical direction. This proved to be inadequate to properly resolve the boundary layer. The difference in predictions between simulations with grid spacing of 0.05 mm and 0.03 mm is

negligible (< 0.1%). Therefore, the solution is independent of grid size when the spacing is smaller than 0.05 mm. The maximum Courant number was limited to 0.3 in the simulations. The simulation results were insensitive to the time step when the Courant number was below this value.

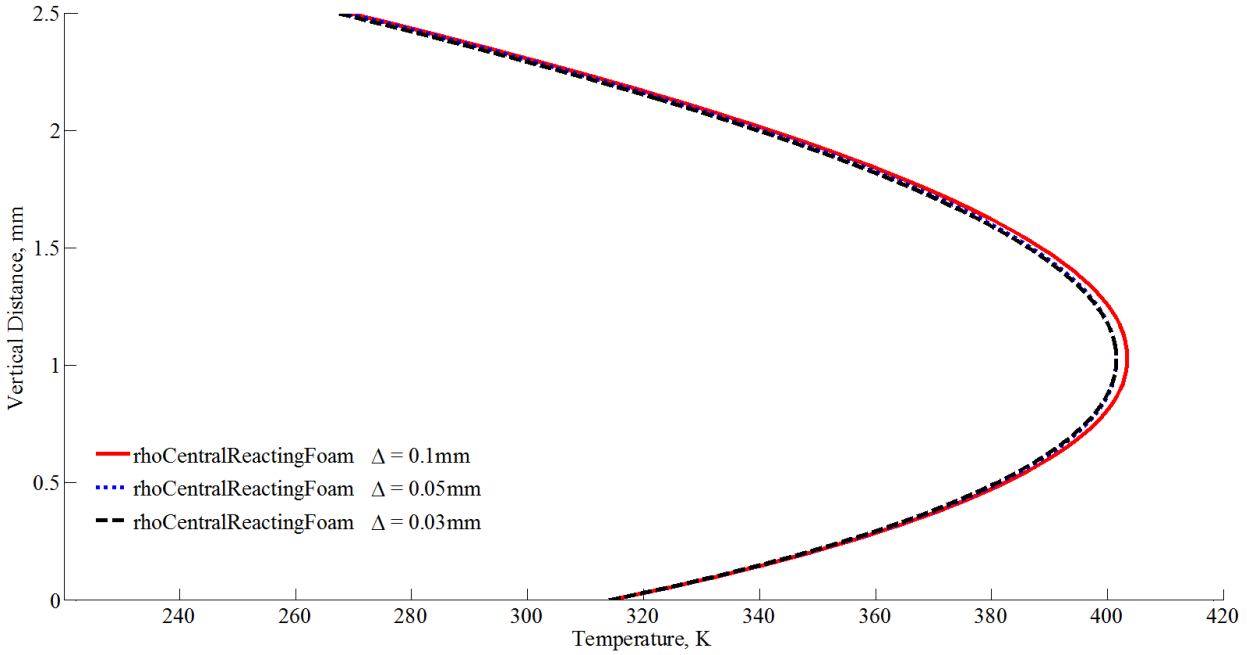

Figure 3.3: Grid convergence and boundary layer resolution. x = 106 mm downstream of leading edge.

Greenshields *et al.* recommends that a limited van Leer interpolation scheme be used when using rhoCentralFoam (Greenshields et al., 2010). However, it was found that the use of the van Leer limiter results in an oscillatory solution, which is most noticeable for the x velocity in the post-shock region. Therefore, a Gamma differencing scheme was used instead as it maintained steep gradients near the shock but eliminated oscillations (Jasak, Weller, & Gosman, 1999). Figure 3.4 shows a plot of the x velocity along the x axis at approximately half the computational domain height (y = 15 mm) comparing the vanLeer limiter and Gamma differencing schemes. As

can be seen from the figure, the vanLeer limited solution oscillated considerably; these oscillations did not decay as the simulation time increased.

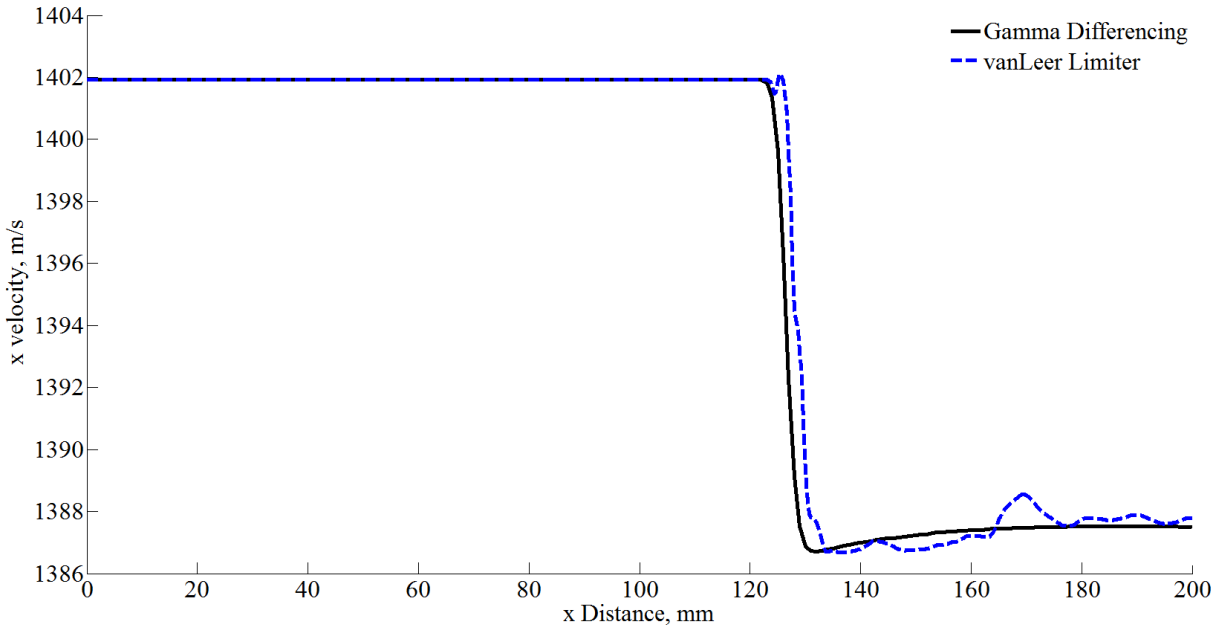

Figure 3.4: vanLeer Limiter and Gamma differencing numerical interpolation schemes for a 5 degree wedge, Pstag = 350psi; Tstag = 1000K.

3.4 **Solution Comparisons**

3.4.1 To previous work

Simulation results from rhoCentralReactingFoam are compared directly against the previous work done in ANSYS® Fluent v6.3 (C. Johansen & Danehy, 2012). Figure 3.5 shows contours of Mach number over the computational domain for the simulation with no gas seeding. The major flow features of note are the boundary layer and oblique shockwave that form in the flow.

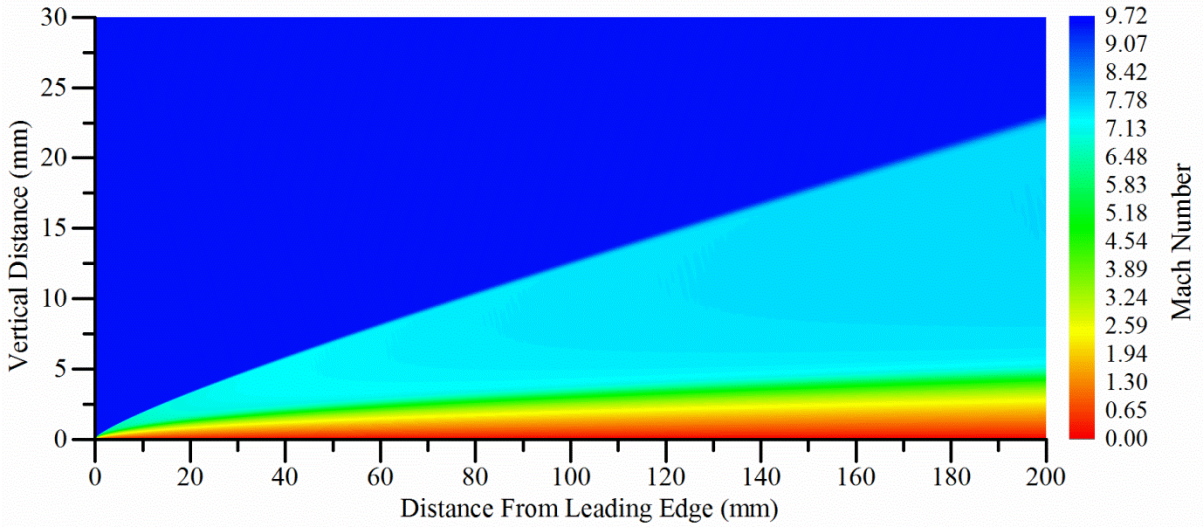

Figure 3.5: Contours of Mach number predicted by rhoCentralReactingFoam. No gas seeding

Figure 3.6 shows comparisons of vertical distributions of Mach number, pressure and temperature for the same case with no gas seeding. Consistent with the previous work, the vertical (y) distributions are displayed at a streamwise position of x = 106 mm downstream of the leading edge. This position corresponds to the location of a supersonic pitot rake used in the experiments.

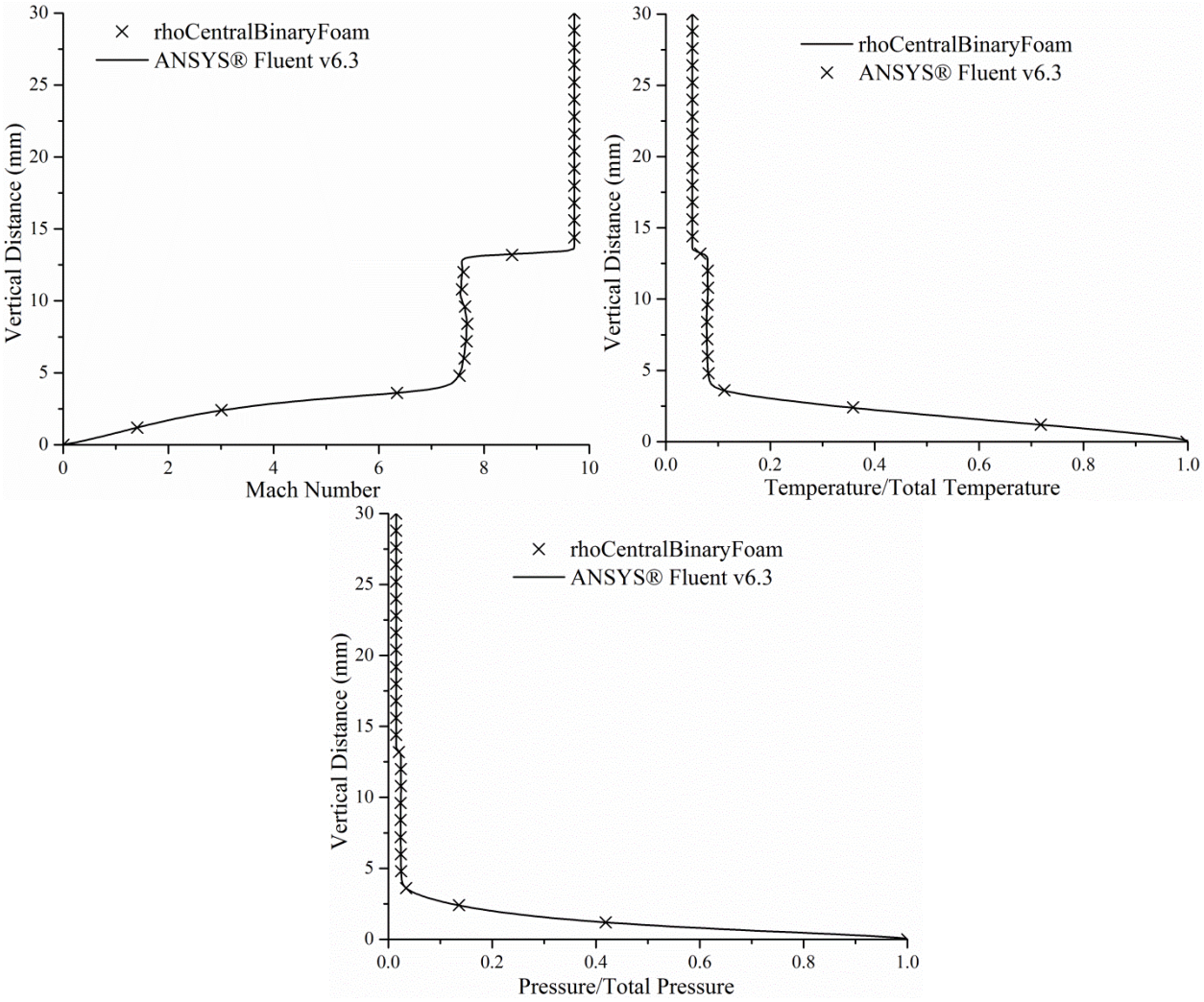

Figure 3.6: Vertical distributions of Mach number (top left), Temperature/Total Temperature (top right) and Pressure/Static Pressure (bottom) predicted by rhoCentralReactingFoam and ANSYS® Fluent. x = 106 mm downstream of leading edge. No gas seeding

In general, there is good agreement between the rhoCentralReactingFoam code and ANSYS® Fluent in predicting mean flow quantities.

RhoCentralReactingFoam's binary diffusion model was also compared to ANSYS® Fluent. Both solvers computed NO, I_2 and Kr seeding into the boundary layer using the same freestream conditions. This comparison is done for both a mass flow rate of 3 mg/s and for the case where

the mass flow rate was zero but mass was allowed to enter the domain via diffusive flux at the jet boundary. The comparison can be seen in Figure 3.7.

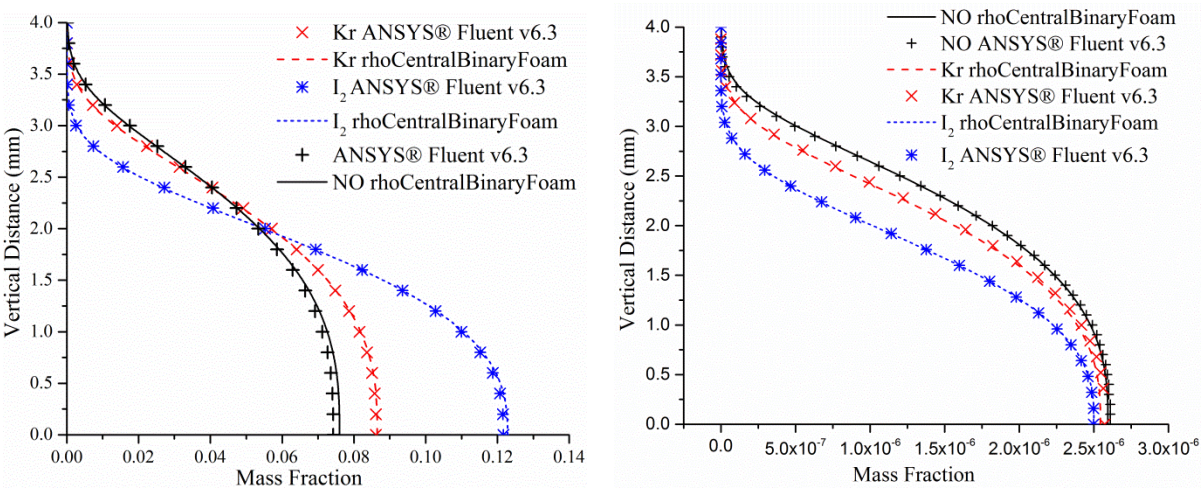

Figure 3.7: Vertical distributions of NO mass fraction predicted by rhoCentralReactingFoam and ANSYS® Fluent. x = 106 mm downstream of leading edge. NO mass flow rate = 3 mg/s (left), diffusive flux only (right)

Although excellent agreement between bulk flow properties is demonstrated, there are slight differences near the wall. These differences are suspected to be due to the different mass flow boundary conditions between the two codes. The Fluent simulations specify an average mass flux over the boundary where OpenFOAM specifies a mass flow rate. Slight differences between the two methods of controlling the mass flow are suspected to be responsible for the differing wall concentrations as this difference is not present in the diffusive flux only case. The maximum deviation between the two codes over the entire boundary is less than 5%, with the maximum located at the outflow boundary. The discrepancy between the two codes has negligible impact on the simulation results outside the wall concentration and do not affect the conclusions of the study.

3.4.2 To Experimental Results

To assess the validity of the computation results, a comparison with experiments performed in the 31-Inch Mach 10 Air Blowdown facility using the 20 degree wedge model is made. The first validation effort involves comparison of computed versus experimental streamwise velocity profiles. The experimental profiles were obtained using NO PLIF MTV during a single run in the wind tunnel. Details regarding the NO PLIF MTV technique can be found in Bathel et al. (2010). The profiles extend in the wall-normal direction and were obtained at multiple streamwise locations above the wedge model surface. A nominal NO mass flow rate of $\dot{m}_{NO}$ = 3 mg/s was used to seed the boundary layer. Figure 3.8 shows the comparison between the computed (solid curves) and experimental (black points) streamwise velocity profiles. The vertical red lines correspond to the streamwise origin of each profile. Computed profiles both with (blue) and without (green) simulated NO seeding are presented. The centers of the horizontal black data points corresponds the measured mean streamwise velocity while the width corresponds to the uncertainty in the mean. For these data, a total of 183 single-shot images were acquired to calculate the experimental streamwise velocities and uncertainties. In some instances, especially near the edge of the boundary layer, low signal-to-noise limited the number of single-shot measurements used to calculate a mean streamwise velocity. Near the model wall, laser scatter off of the model surface prevented a useful measurement of streamwise velocity. Over the course of the run, a small physical downward displacement of the model was observed. Presumably, the displacement is a result of non-uniform mechanical and thermal loading on the sting. The plate surface was also rotated approximately 0.15° with respect to the horizontal axis of the camera. To correct for the displacement and rotation, the raw images were translated upward and rotated

clockwise using the MATLAB® function *imwarp* with cubic interpolation. The uncertainty in the wall-normal placement of the experimental data points is estimated to be ±0.13 mm.

Figure 3.8 shows that the best agreement with experiment occurred for the computation with a simulated $\dot{m}_{NO}$ = 3 mg/s seed (blue curves). Relative to the computation with no seed (green curves), both the experimental measurements and computation with seeding exhibit a velocity deficit and increased thickness. This result is to be expected, as the seeding alters the streamwise momentum of the boundary layer.

A second validation consists of a comparison between the computed and experimental wall pressure at a point 33 mm downstream of the leading edge. This comparison is used to determine if the computed flowfield accurately captures the leading edge hypersonic viscous interaction. For this second comparison, the average measured wall pressure from five separate wind tunnel runs was computed. Each average measurement was computed after the wall pressure sensor (Druck PDCR 4060, 0.04% accuracy up to 34.5 kPa) reading stabilized. The mean wall pressure of the five runs was then computed along with the uncertainty in the mean. Figure 3.9 shows the mean wall pressure measurement divided by the estimated post-shock far-field pressure obtained with an inviscid oblique shock calculation. This measurement is plotted against the streamwise wall pressure distribution divided by the post-shock far-field pressure (200.9 Pa). This computed pressure distribution is along the model centerline with no simulated seeding. As can be seen, the simulation (solid curve) accurately predicts the elevated wall pressure caused by the viscous interaction. The dashed curve in this figure represents the pressure ratio in the absence of a hypersonic viscous interaction.

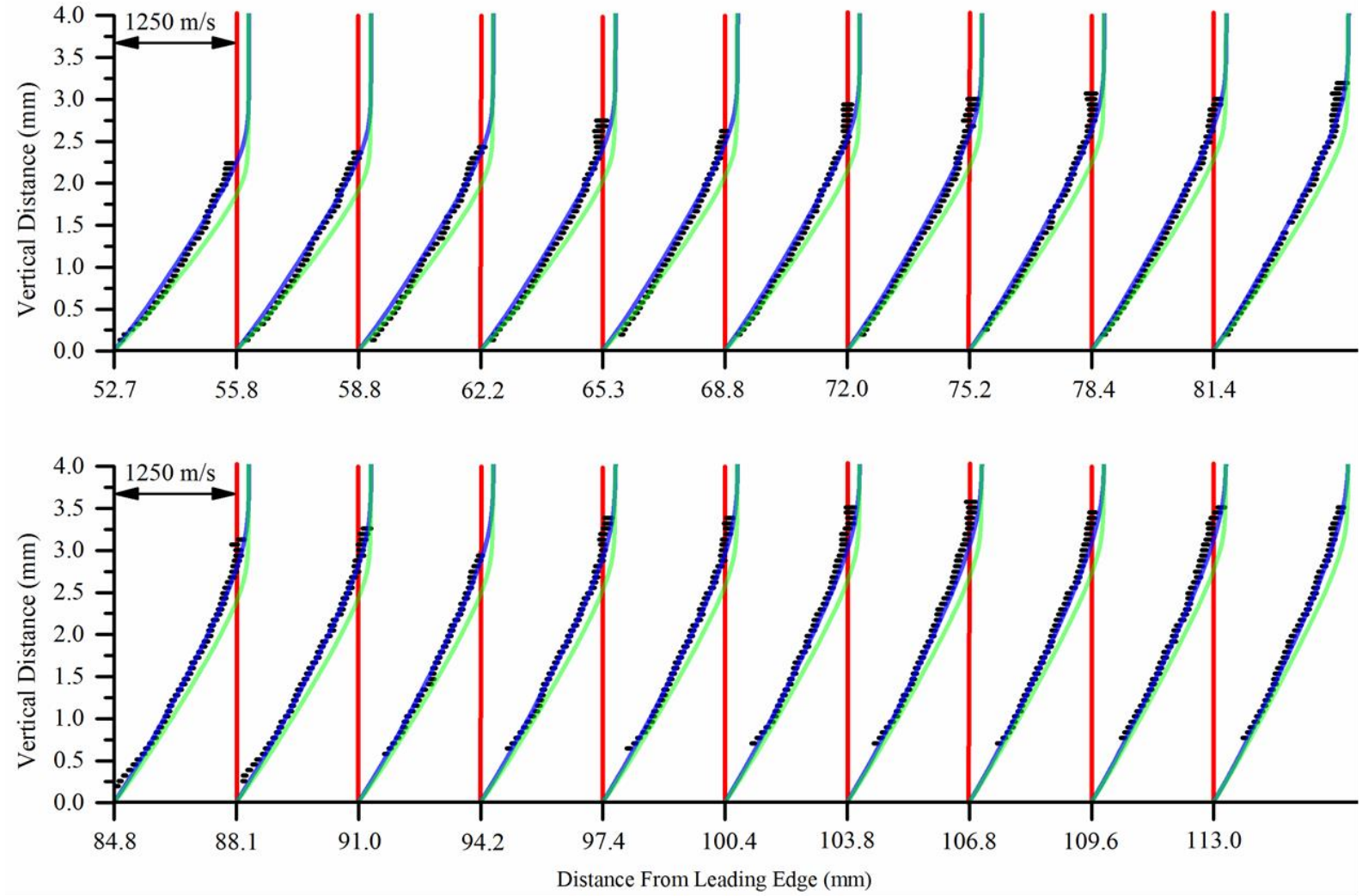

Figure 3.8: Comparison of computed and experimental (black points) streamwise velocity profiles. Computed profiles are with seeding (blue) and without seeding (green); NO mass flow rate = 3 mg/s

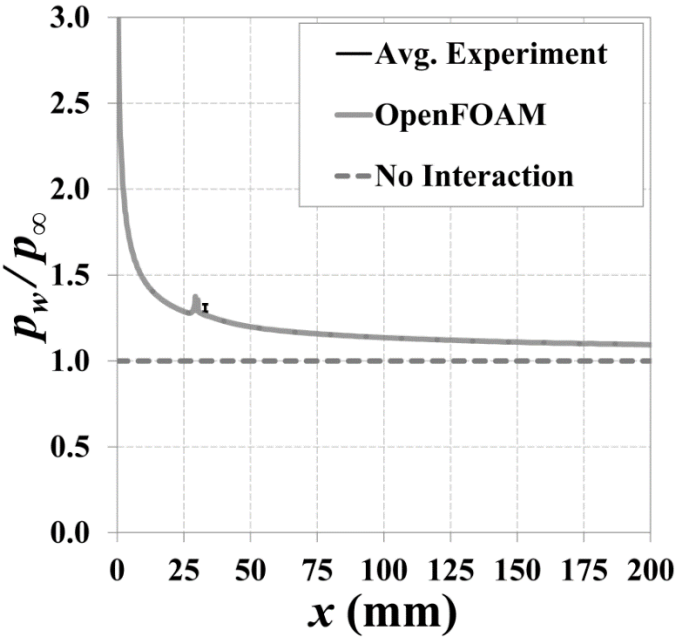

Figure 3.9: Comparison of computed streamwise wall pressure along the model centerline with measured mean wall pressure

3.4.3 To Ideal Profile

It is also advantageous to compare the simulation results for the three seed gasses to an idealized profile. From a PLIF perspective a uniform signal is desired across the region being investigated. In this case that region corresponds to the boundary layer. In this idealization a uniform signal was assumed to be generated by a uniform concentration of seed gas across the boundary layer. This assumption neglects a number of effects including the temperature dependence of PLIF signal, quenching, and radiative trapping. In order to take these effects into account models relating the effects back to the simulation data would be required, which complicates the analysis beyond the scope of this work. However comparing the results to a uniform concentration does yield some useful insight.

The ideal profiles were calculated by averaging the total number of mols in a given vertical slice over the boundary layer thickness:

$$\mathrm{n_{ideal}} = \frac{1}{\delta}\int_0^{\delta} n_{sim}\,dy \tag{3.11}$$

where δ is the boundary layer thickness and n is the number of mols of the seed gas in the ideal and simulated cases. The overall difference between ideal and simulated profiles as a function of streamwise position, normalized by boundary layer thickness, can then be defined as:

$$\mathrm{error} = \frac{1}{\delta}\int_0^{\delta} |n_{ideal} - n_{sim}|\,dy|_x \tag{3.12}$$

Shown in Figure 3.10 is the difference between the ideal profile and the simulated profile as a function of streamwise distance from the leading edge. Interestingly I_2 appears to have the lowest difference from the idealized profile. This is of note because in previous studies NO was found to be the ideal seed gas for this type of seeding (C. Johansen & Danehy, 2012). I_2 has the lowest difference from the idealized profile because I_2 disperses slower than NO and therefore has a more uniform profile. The profiles also all appear to approach a relatively similar difference between the simulated and ideal profiles at the edge of the computational domain with the differences between the three becoming less notable.

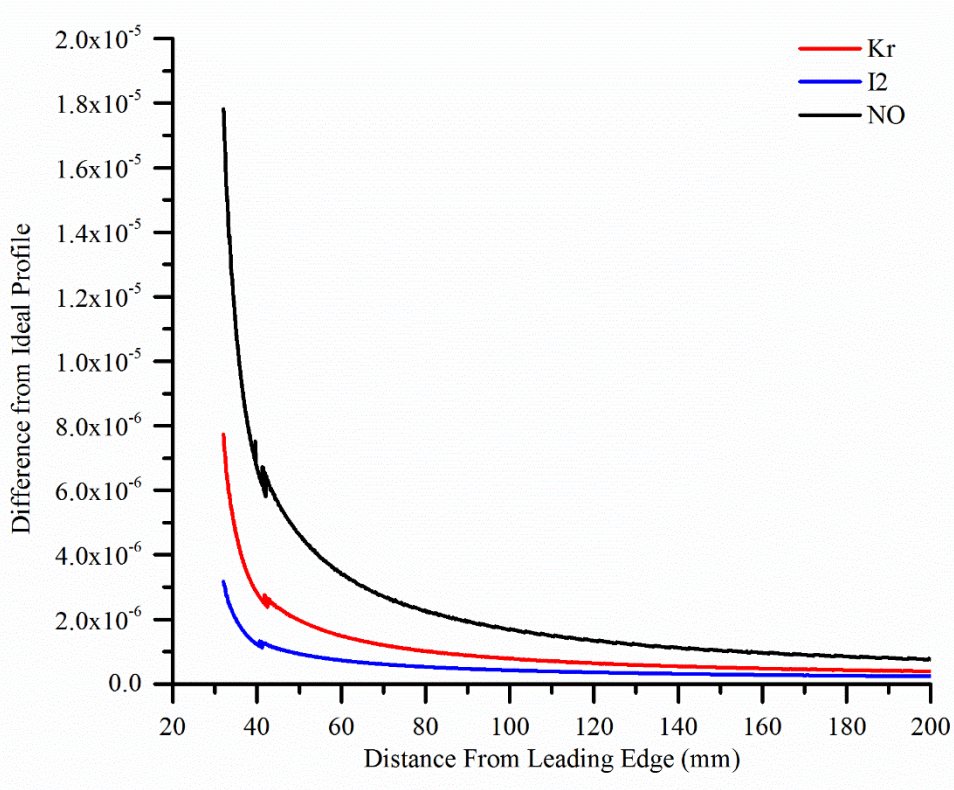

Figure 3.10: Difference from ideal profile; seed gas flow rate = 3 mg/s

Shown in Figure 3.11 is the concentration profile for the three gasses at the edge of the computational domain (x = 200 mm downstream of the leading edge). Because of the velocity boundary layer, most of the seed gas gets entrained near the wall. As it diffuses towards the edge of the boundary layer it gets swept away by the higher velocities. This leads to a sharper and less uniform concentration profile for Kr and NO when compared to I_2 as these gasses diffuse faster than I_2. Also shown in the figure is the boundary layer thickness at that location.

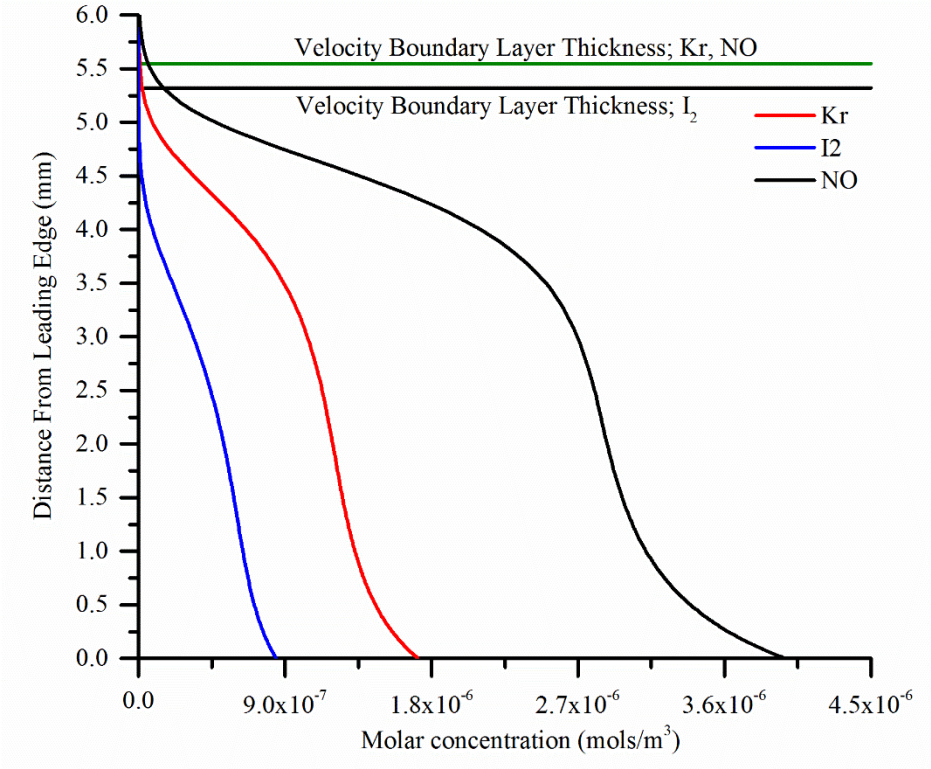

Figure 3.11: Molar concentration; x = 200 mm downstream from leading edge; seed gas flow rate = 3 mg/s

While I_2 has a more idealized profile it comes at the cost of boundary layer penetration. NO has the best penetration into the velocity boundary layer and is the only gas that actually diffuses beyond the velocity boundary layer which, as mentioned previously, is very desirable when selecting a seed gas for this type of experiment. As a result there exists a tradeoff between boundary layer penetration and the idealized profile. However since NO is the only gas that penetrates beyond the velocity boundary layer it remains the best choice for this type of boundary layer seeding experiment.

Chapter 4: Slip Effects

There exists a potential for localized slip effects at the wall in the simulations. While the freestream Knudsen number based on plate length is approximately Kn = 0.003, the Knudsen number at the wall based on boundary layer thickness varies such that rarefied effects may be significant near the leading edge where the boundary layer thickness is relatively small. As a result, the impact of slip at the wall on the simulation results needs to assessed. An estimate of the slip velocity can be obtained using the first order (Maxwell) slip model (Kennard, 1938):

$$u_{slip} = \frac{2 - \sigma_u}{\sigma_u} \lambda \frac{\partial(u)}{\partial y} \tag{4.1}$$

where λ is the mean free path. σ_u is the accommodation coefficient and is the proportion of molecules reflected diffusely or specularly from the surface. For this work the accommodation coefficient was assumed to be equal to one which corresponds to all molecules being reflected from the surface diffusely. Under this assumption the Maxwell slip equation reduces to:

$$u_{slip} = \lambda \frac{\partial(u)}{\partial y} \tag{4.2}$$

The mean free path was estimated by (Vincenti & Kruger, 1986):

$$\lambda = \frac{1}{\pi \sum_{s,i} n_i d_{s,i}^2 \sqrt{1 + \left(\frac{m_s}{m_i}\right)}} \tag{4.3}$$

where n_i is the number density of species i, m_s is the mass of the seed molecule, m_i is the mass of the collision partner molecule, $d_{s,i}$ is the average collision diameter. The slip velocity was estimated using a combination of the above equations and the results from the no-slip simulation with NO seeded at 3 mg/s. A distribution of the slip velocity is shown in Figure 4.1.

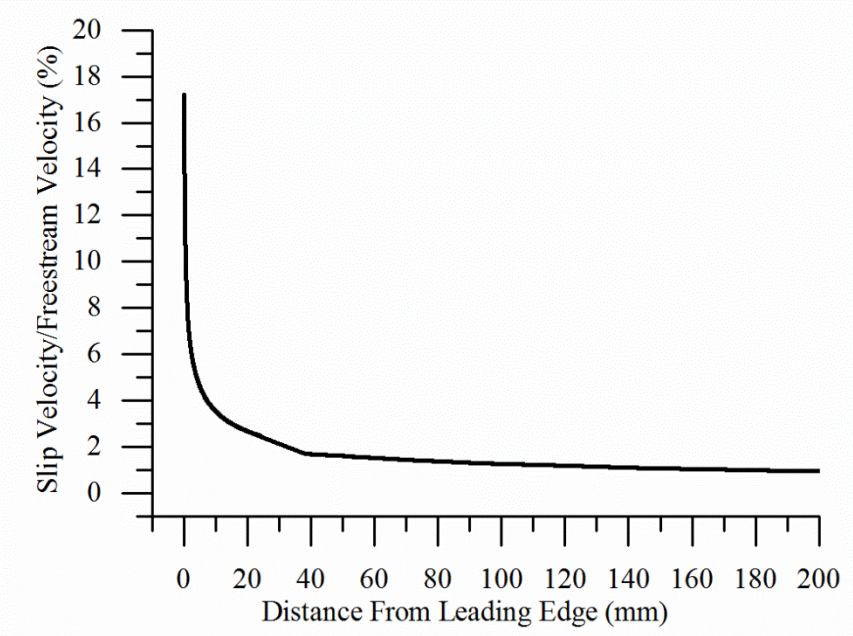

Figure 4.1: Estimated streamwise distribution of slip velocity along the wedge. NO seeded at mass flow rate = 3mg/s

From the figure it can be seen that the slip velocity is nearly negligible downstream of the gas seed slot. This means that the localized slip in that region should have very little impact on the no-slip results. However, there are large amounts of predicted slip (>15%) near the leading edge. This slip has the potential to alter the shock angle and thereby alter the post-shock free stream values and the seed gas distribution.

A simulation was performed to quantify the effect of the localized slip at the leading edge. The simulation prescribed the predicted slip velocity shown in Figure 4.1 along the bottom boundary of the wedge through a fixed velocity boundary condition. This was done for the case with NO seeded at a mass flow rate equal to 3 mg/s.

Results from the slip simulation are shown as a Mach number contour in Figure 4.2 and are compared to the no-slip case. The figure has been zoomed in on the leading edge for visibility.

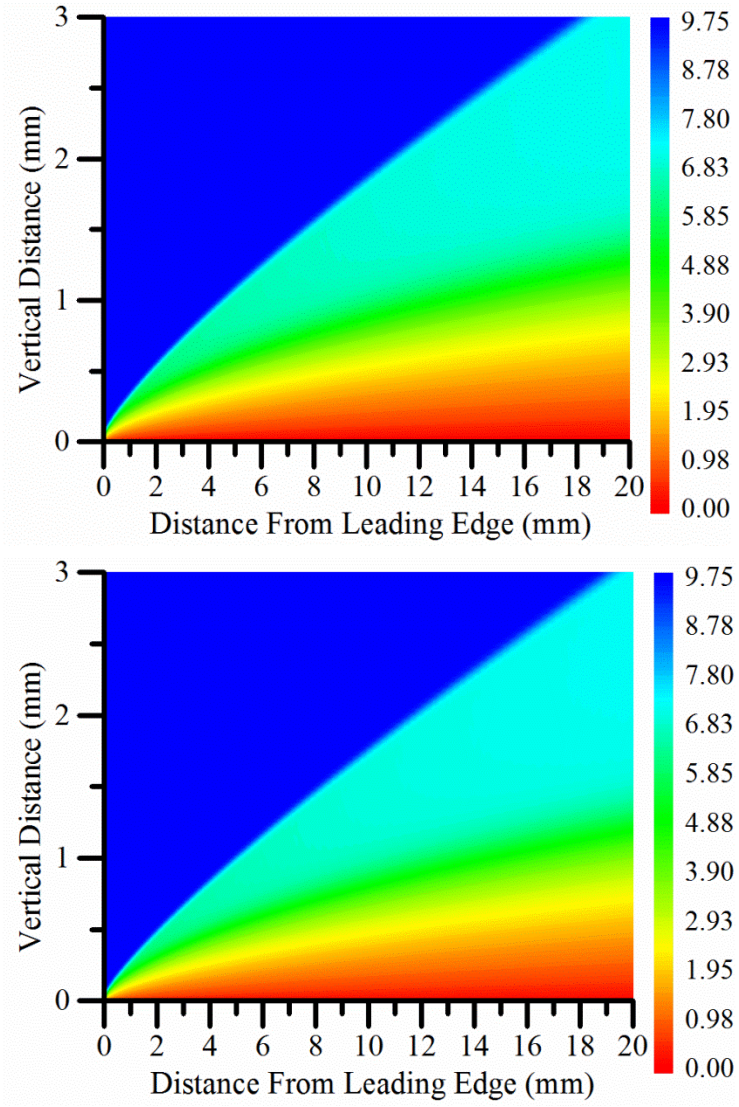

Figure 4.2: Contours of Mach number. No-slip (top) and slip (bottom) simulations

From Figure 4.2 it can be seen that the slip at the leading edge reduces the thickness of the shock layer slightly, changing the location of the shock. This is expected as the slip velocity at the wall would effectively decrease the boundary layer thickness. Interestingly, under these conditions, the shock angle remains unchanged. This is indicated by the post shock free stream values being the same for both the no-slip and slip cases.

The viscous leading edge effects also remain unaltered downstream of the leading edge. This is shown in Figure 4.3 which shows the wall pressure distribution for the slip and no slip cases. The wall pressure has been normalized by P_{inf}, which is the inviscid post-shock freestream pressure calculated using the oblique shock relations (J. John & Keith, 1984). As is expected, the peak pressure at the leading edge decreases in the slip simulation (1311 – 890 Pa) but downstream of the leading edge the wall pressure is equal for both cases.

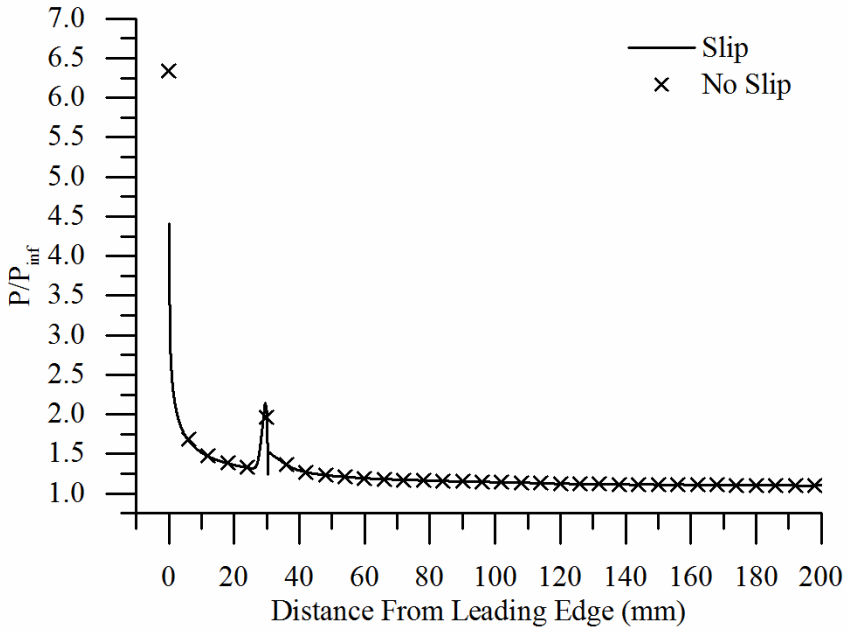

Figure 4.3: Wall pressure distribution comparison between No-slip and slip simulations

Shown in Figure 4.4 are vertical distributions of streamwise velocity at x = 3, 20 and 106 mm downstream of the leading edge. The wall slip velocity does slightly decrease the boundary layer thickness. This is because the freestream velocity remains relatively constant while the wall has a slight nonzero velocity. This is most notable near the leading edge where the slip velocity is high. However, the difference in boundary layer thickness becomes negligible further

downstream. This is indicated by the vertical distribution 20 and 106 mm downstream of the leading edge.

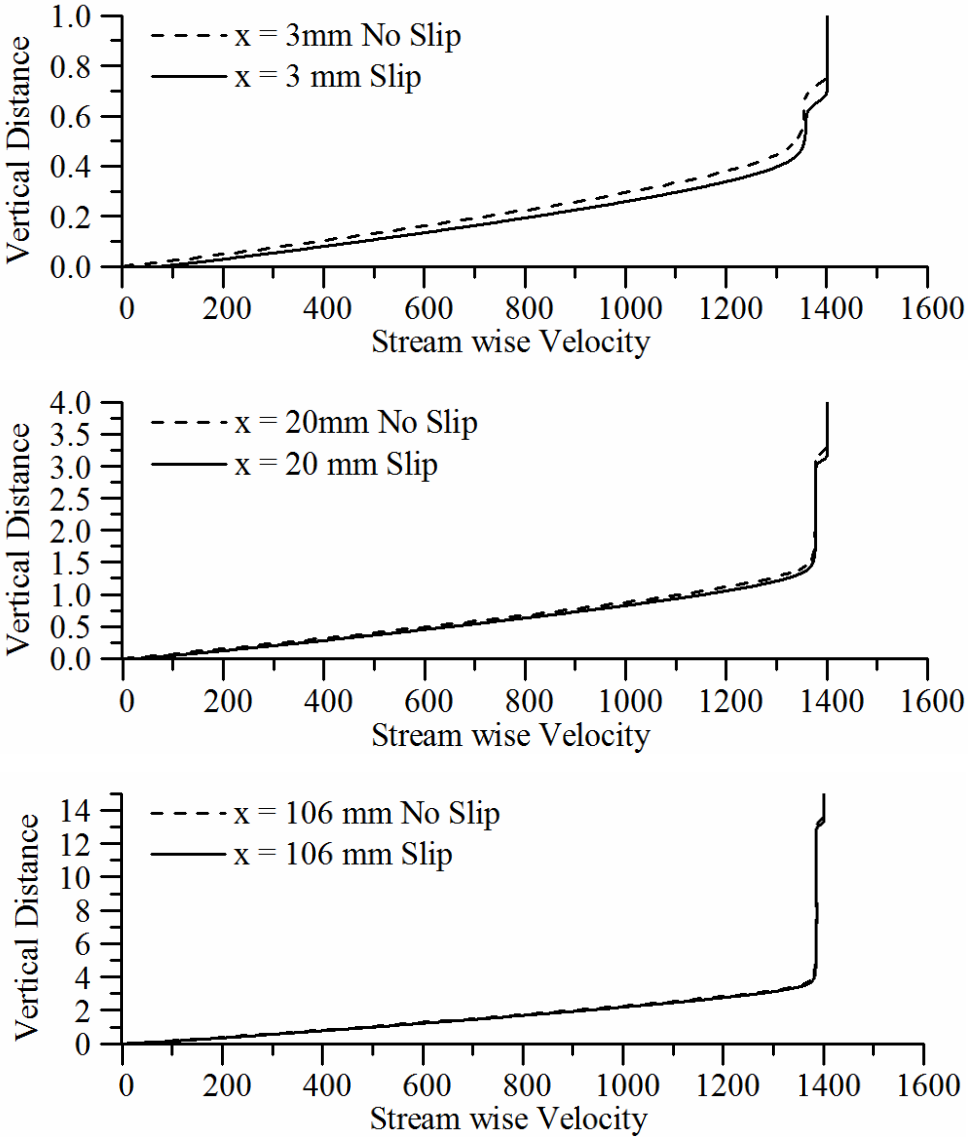

Figure 4.4: Vertical distributions of streamwise velocity, x = 3 mm (top) x =20 mm (middle) x = 106 mm (bottom)

Chapter 5: NO Chemistry

Although NO forms naturally in the stagnation chamber of the 31-inch Mach 10 facility, there is no detectable quantity of NO in the test section. The static temperature in the freestream of the test section drops to approximately 52 K because of a large expansion that occurs in the nozzle. Rapid, low temperature reactions are thought to destroy NO before it can reach the test section. NO reacts with O_2 at low temperatures in a termolecular exothermic reaction to form nitrogen dioxide (NO_2) defined as:

$$O_2 + 2NO => 2(NO_2) \tag{5.1}$$

There is a concern that the reaction of the locally seeded NO with surrounding oxygen will alter the thermodynamic properties of the boundary layer. The reaction rate has been measured experimentally by Olbregts (1985). An adapted version of his empirical formula in an Arrhenius rate form is given as:

$$k_{NO} = 10^{A}T^{B} \exp\left[\frac{E_a}{RT}\right] \tag{5.2}$$

where E_a is the activation energy given by

$$E_a = RCln(10) \tag{5.3}$$

A, *B*, and *C* are empirical constants with values of -5.18, 2.70 and 700, respectively. The formula given in Eq. (5.2) has units of liters^2 mols^{-2} seconds^{-1}. A plot of the reaction rate as a function of temperature is shown in Figure 5.1. The empirical formula is valid for temperatures between 226 K and 758 K (Olbregts, 1985).

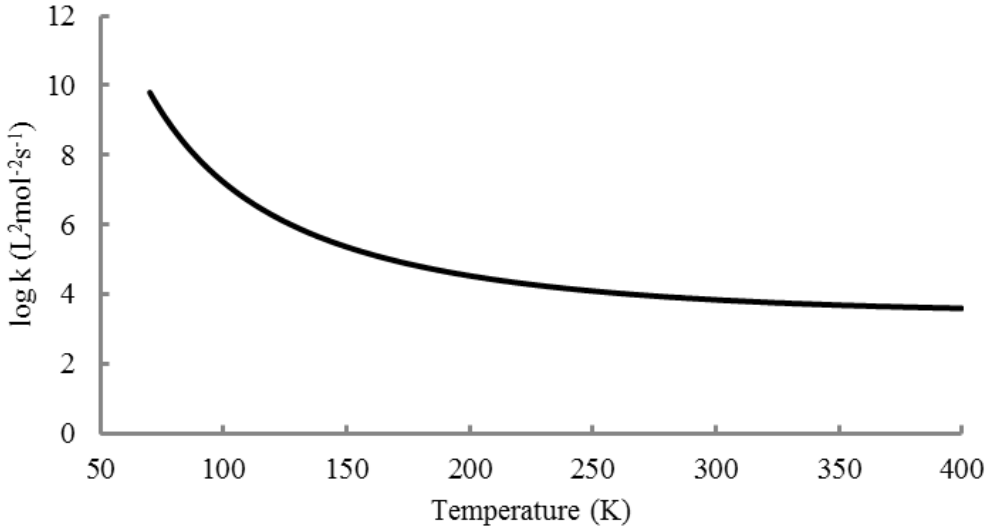

Figure 5.1: Effect of temperature on rate of reaction of NO.

In the following calculations, the reaction rate model was extrapolated to low temperatures to account for the relatively cold edge conditions near the edge of the boundary layer. However, the temperature in the boundary layer where most of the NO is concentrated is approximately 300 K to 400 K in the 5 degree case.

5.1 **NO Half-life**

The importance of NO chemistry in the flow was estimated through a half-life calculation. The half-life is then compared to the residence time of the flow based on analytical pressure, temperature, and velocity calculations. Finally, the half-life calculation is applied to CFD simulations with and without gas seeding. The change in NO concentration over time can be written as:

$$\frac{d[NO]}{dt} = -2k_{NO}[O_2][NO]^2 \tag{5.4}$$

If the concentration of O_2 is allowed to vary, the change in O_2 concentration over time can be written as:

$$\frac{d[O_2]}{dt} = -k_{NO}[O_2][NO]^2 \tag{5.5}$$

substituting Eq. (5.5) into Eq. (5.4) gives:

$$\frac{d[O_2]}{dt} = \frac{1}{2}\frac{d[NO]}{dt} \tag{5.6}$$

assuming O_2 is in excess $[O_2]$ can be written as:

$$[O_2] = [O_2]_u + [O_2]_e \tag{5.7}$$

where $[O_2]_u$ is the concentration of O_2 used by the reaction and $[O_2]_e$ is the excess concentration of O_2. From Eq. (5.1) the ratio of NO to O_2 used can be obtained. Solving Eq. (5.7) for $[O_2]_u$ and substituting into this ratio results in:

$$\frac{[NO]}{[O_2] - [O_2]_e} = 2 \tag{5.8}$$

solving Eq. (5.8) for $[O_2]$ and substituting into Eq. (5.5) yields:

$$\frac{d[NO]}{dt} = -2k_{NO}\left(\frac{[NO]^3}{2} + [NO]^2[O_2]_e\right) \tag{5.9}$$

separating variables results in:

$$\frac{d[NO]}{\frac{[NO]^3}{2} + [NO]^2[O_2]_e} = -2k_{NO}dt \tag{5.10}$$

since $[O_2]_e$ is a constant, Eq. (5.10) can be integrated:

$$-2k_{NO}t_{1/2} = \frac{[NO]_i\, ln\left[\frac{[NO]_i + 4[O_2]_e}{[NO]_i + 2[O_2]_e}\right] - 2[O_2]_e}{2[O_2]_e^2[NO]_i} \tag{5.11}$$

Knowing that the excess concentration of O_2 is equal to the initial concentration less the used concentration and that the ratio of O_2 used to NO is equal to two; the excess concentration of O_2 can be written as:

$$[O_2]_e = [O_2]_i - \frac{1}{2}[NO]_i \tag{5.12}$$

The concentrations of NO and O_2 can be written as:

$$[NO] = X_{NO}\left(\frac{P}{RT}\right) \tag{5.13}$$

$$[O_2] = X_{O_2}\left(\frac{P}{RT}\right) \tag{5.14}$$

From Eq. (5.13) and Eq. (5.14), Eq. (5.12) can be written as:

$$[O_2]_e = \left(X_{O2,i} - \frac{1}{2}X_{NO,i}\right)\left(\frac{P}{RT}\right) \tag{5.15}$$

Substituting Eq. (5.13) and Eq. (5.15) into Eq. (5.11) and solving for $t_{1/2}$ results in:

$$t_{1/2} = \frac{R^2T^2}{P^2}\,\frac{X_{NO,i}\left(1 + ln\left[\frac{4X_{O2,i} - X_{NO,i}}{2X_{O2,i}}\right]\right) - 2X_{O2,i}}{-k_{NO}\left(2X_{O2,i} - X_{NO,i}\right)^2 X_{NO,i}} \tag{5.16}$$

where *X* is the mol fraction of the subscript species. Assumed in the derivation of the above half-life expression is that O_2 is in excess and varies as the reaction proceeds. Once the half-life of NO is known it can be compared to the residence time in the computational domain. If the half-life is long compared to the residence time of the flow then the flow can be approximated as non-reacting. Figures 5.2 and 5.3 show contour plots of temperature and pressure obtained from the OpenFOAM simulation with no gas seeding. Pressure and temperature are directly related to the reactant concentration and reaction rate. Figure 5.4 shows the ratio of half-life length scale ($L_{1/2}$) normalized by the local simulation length scale (L_{sim}):

$$\frac{L_{1/2}}{L_{sim}} = \frac{U_x * t_{1/2}}{L_d - x} \tag{5.17}$$

where U_x is the *x* velocity, L_{sim} is the remaining length of the computational domain and *x* is the horizontal distance from the origin (leading edge). Because of the large range in $L_{1/2}$ calculations,

Figure 5.4 is shown on a log scale. The half-life length scale was chosen since the reaction is asymptotic at low NO concentrations. It provides an order of magnitude analysis. A large value of $L_{1/2}/L_{sim}$ indicates that the flow is non-reacting. Also of interest in the figures are the various flow features including the oblique shock and the development of the thermal boundary layer.

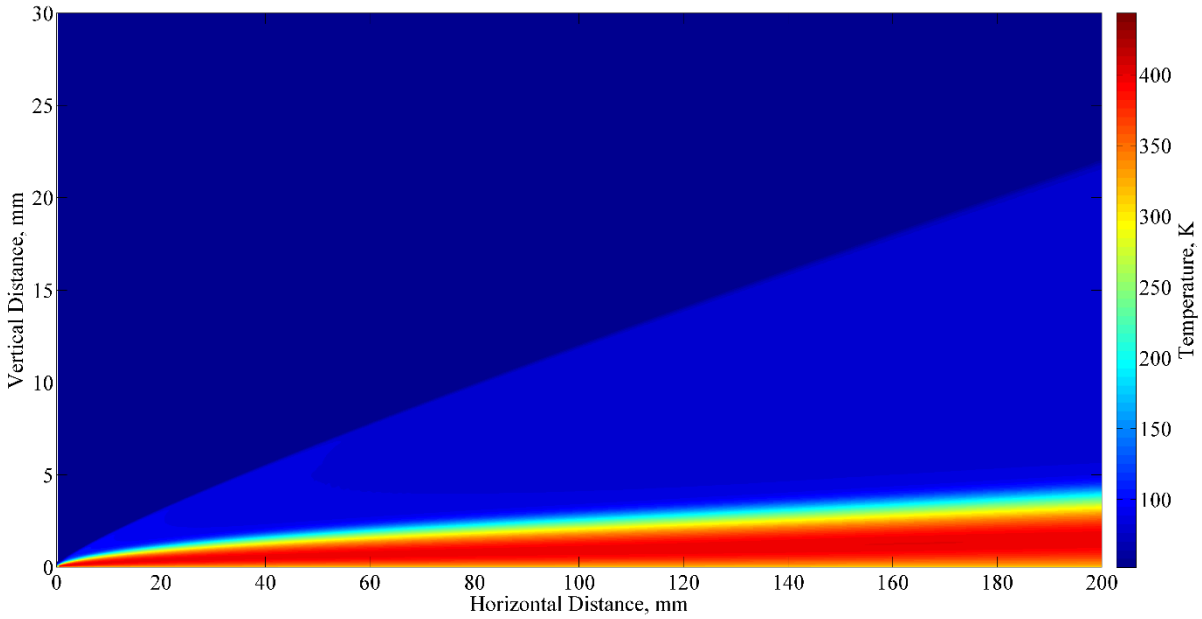

Figure 5.2: Simulated temperature distribution. P_{stag} = 350 psi; T_{stag} = 1000 K; θ_{plate} = 5°.

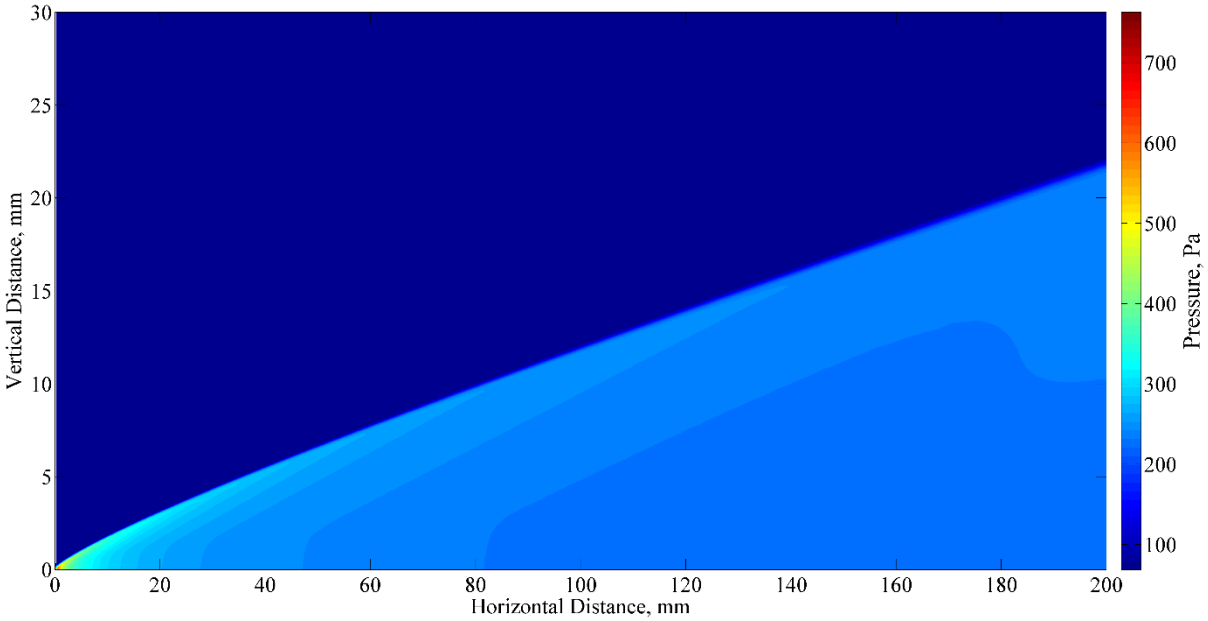

Figure 5.3: Simulated pressure distribution. P_{stag} = 350 psi; T_{stag} = 1000 K; θ_{plate} = 5°.

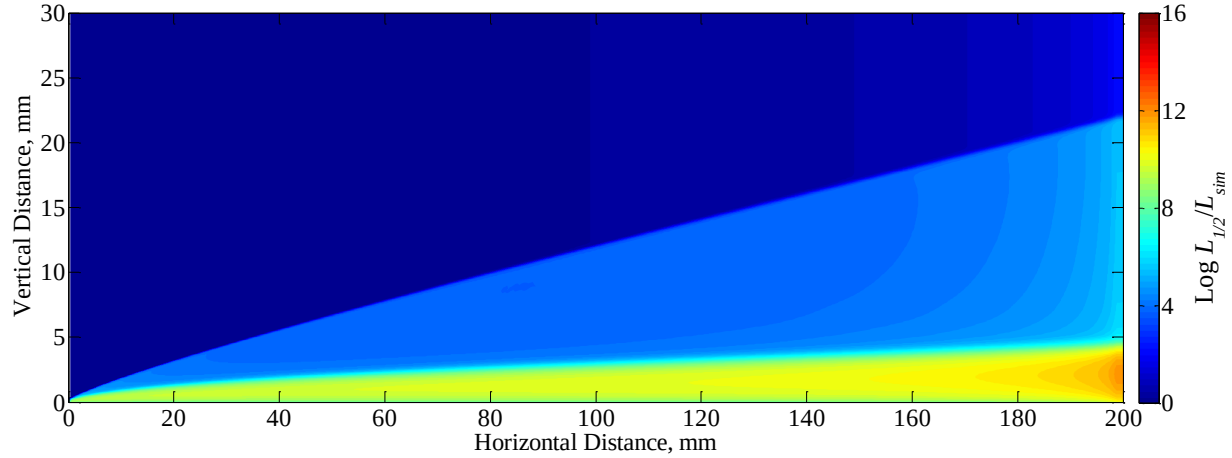

Figure 5.4: Simulated $L_{1/2}/L_{SIM}$ distribution based on Eq. (5.17) P_{stag} = 350 psi; T_{stag} = 1000 K; θ_{plate} = 5° ; $X_{NO,i}$ = 0.1; $X_{O2,i}$ = 0.2.

The minimum value of the $L_{1/2}/L_{SIM}$ ratio is 0.84 and occurs in the freestream at the computational domain inlet where the temperature is 52 K. This indicates that if NO was present in the freestream, it would react within the computational domain. However, NO is seeded at the wall and is unable to penetrate much beyond the velocity boundary layer, which is far away from

the leading shock wave. Therefore, the lowest expected value of $L_{1/2}$ is at the edge of the boundary layer, which roughly corresponds to the edge conditions after the oblique shock wave. The pressure and temperature conditions at this location, neglecting viscous interaction effects, can be found from the oblique shock relations (J. E. A. John & Keith, 2006).

The minimum half-life length scale for different wedge angles and wind tunnel stagnation conditions can then be estimated from the post-shock conditions and Eq. (5.16). The results over the range of typical stagnation pressures in NASA Langley's 31" Mach 10 facility are shown in Figure 5.5. Cases which have been simulated are indicated with filled-in dots. From the figure it can be seen that the NO reaction has the potential to alter the thermodynamic characteristics at shallower wedge angles and at higher stagnation pressures. The dashed line indicates the position $L_{1/2}/L_{sim} = 1$ and corresponds to the approximate limit where NO reactions will occur within the field of view of the wedge model or computational domain. Two major assumptions are that the NO concentration boundary layer is thicker than the thermal boundary layer and that the Olbregts reaction can be reliably extrapolated to these lower temperatures.

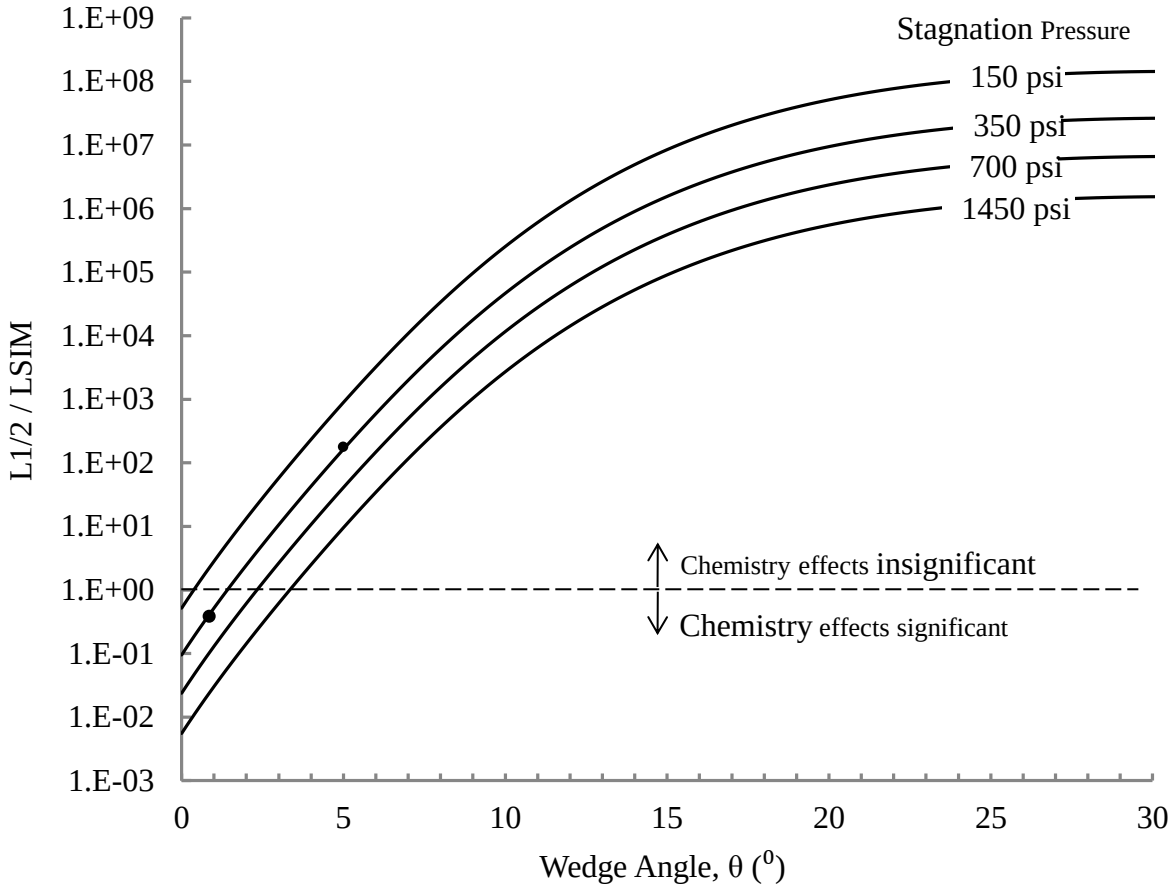

Figure 5.5: Effect of NASA's 31" Mach 10 facility stagnation pressure on the length scales of NO chemistry. Eq. (5.17) used for $L_{1/2}$ calculation.

To account for non-uniform NO distributions, life time calculations were performed on gas seeding simulations without chemical reactions. Figure 5.6 shows the distribution of $L_{1/2}$ based on the simulated NO gas seeding case performed using the rhoCentralReactingFoam solver at a wedge angle of θ_{plate} = 5° and 1° at an NO seed rate of 150 sccm. Also shown on the graphs are isotherms for the thermal boundary layer. The color scheme has been changed from the previous figures to better accentuate the regions where $L_{1/2}$ is at a minimum. It should be noted that the thermal boundary layer continues beyond the isotherms plotted. The oblique shock in the vicinity

of the seed slot makes plotting lower temperature isotherms difficult. The post-shock freestream temperatures are approximately 80 K and 63 K for θ_{plate} = 5° and 1° respectively.

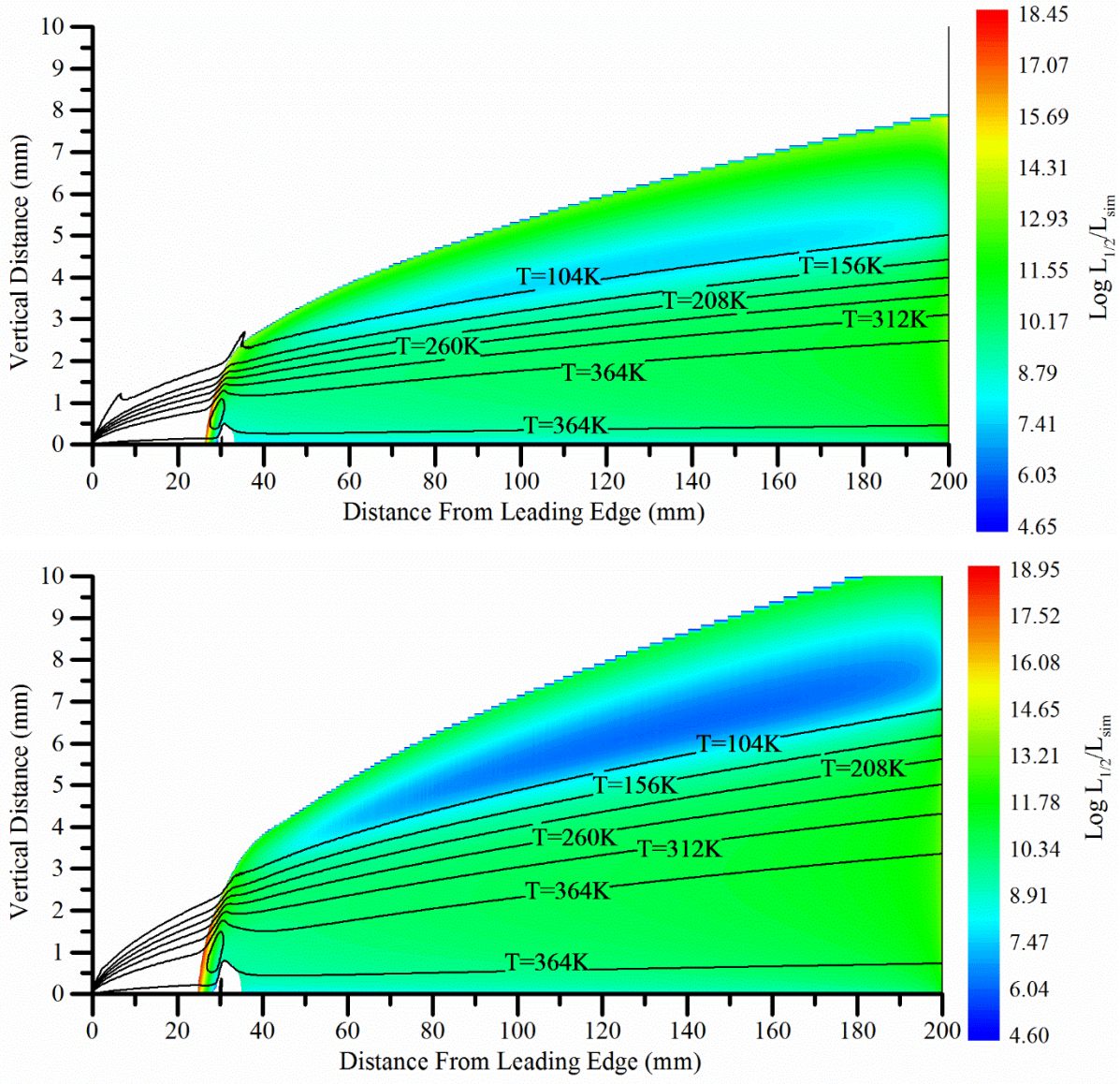

Figure 5.6: $L_{1/2}/L_{SIM}$ distribution based on simulated NO gas seeding and Eq. (5.17) θ_{plate} = 5° (top) 1° (bottom). Isolines of temperature shown.

With gas seeding, the concentration of NO is the largest near the injection slot where the gas temperature is near the wall temperature (314 K). Although the NO reaction rate coefficient, k_{NO},

is large at the edge of the boundary layer, concentration levels of NO decrease such that $L_{1/2}$ values effectively increase. Since there is negligible NO concentration levels outside of the boundary layer, the $L_{1/2}/L_{sim}$ contours were cropped at those locations. For $\theta_{plate} = 5^{o}$, minimum $L_{1/2}$ values occur in the immediate vicinity of the injection slot where the concentration of NO is highest. The next lowest values are near the edge of the boundary layer, where the temperature is low. For $\theta_{plate} = 1^{o}$ the lowest values are near the edge of the thermal boundary layer, but still within it. This is due to the fact that NO does not diffuse beyond the thermal boundary layer in noticeable quantities for either plate angle.

5.2 **Reacting Simulation Results**

Simulations of NO gas seeding with chemical reactions were performed with rhoCentralReactingFoam at a plate angle of 5 degrees and a stagnation pressure of 350 psi. A contour plot of the NO_2 mass fraction with overlaid isotherms is shown in Figure 5.7. As expected, most of the NO_2 forms near the seed slot with some additional NO_2 forming near the edge of the boundary layer. Peak NO_2 locations correspond reasonably well with the predicted minimum $L_{1/2}/L_{sim}$ values shown in Figure 5.6. It was found that the heat release from these reactions had a negligible impact on the temperature distribution. Note that the production of N_2O_4 from NO_2 in an exothermic reaction was not included in this work. The limiting reaction at these conditions is the conversion of NO and O_2 into NO_2. Even when assuming that all of the NO_2 produced converts immediately to N_2O_4, the additional heat generated is not sufficient to have any discernable impact on the flow.

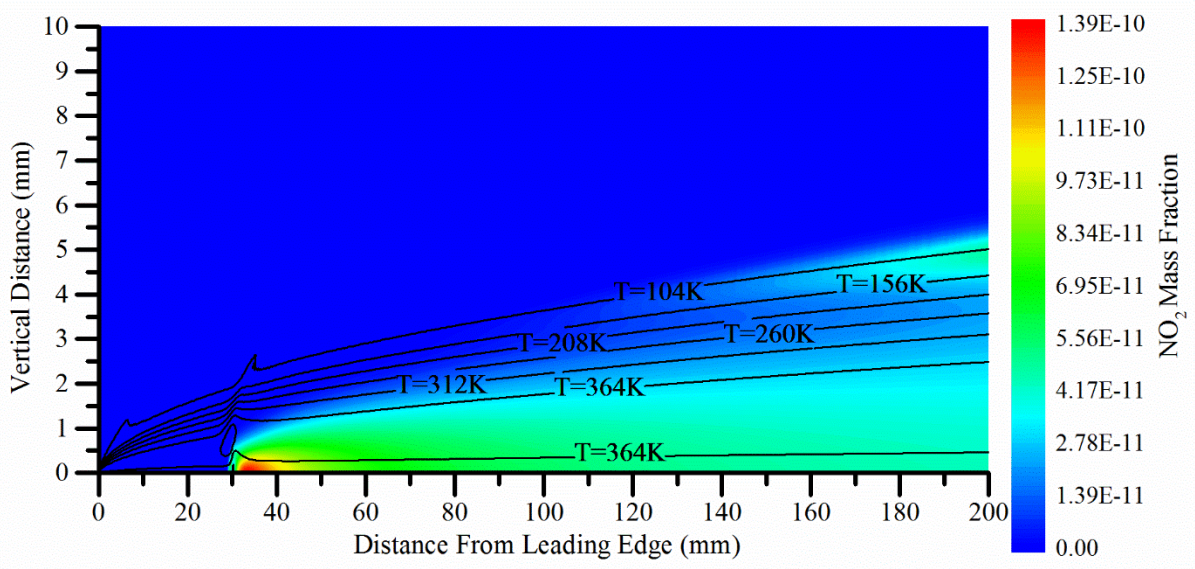

Figure 5.7: Simulated NO_2 distribution P_{stag} = 350 psi; T_{stag} = 1000 K; θ_{plate} = 5° ; Isolines of temperature shown.

Simulations at lower plate AoA (θ_{plate} = 1°) were also performed. It was expected that the lower static temperature at the boundary layer edge would increase the reaction rate. The predicted NO_2 contours at this condition are shown in Figure 5.8. As expected, peak NO_2 concentrations are highly correlated with predicted minimum $L_{1/2}/L_{sim}$ values (Figure 5.6), which occurs at the edge of the thermal boundary layer. However, since concentration levels of NO decrease rapidly downstream of the seeding slot, the effect of chemical reactions on the temperature distribution is still negligible. Although possible in the Langley 31" Mach 10 facility, negative plate angles were not simulated in this study. Small aerodynamic perturbations in the boundary layer were observed as a result of the NO injection. This effect was already reported in a previous study of non-reacting gas seeding simulations (C. Johansen & Danehy, 2012).

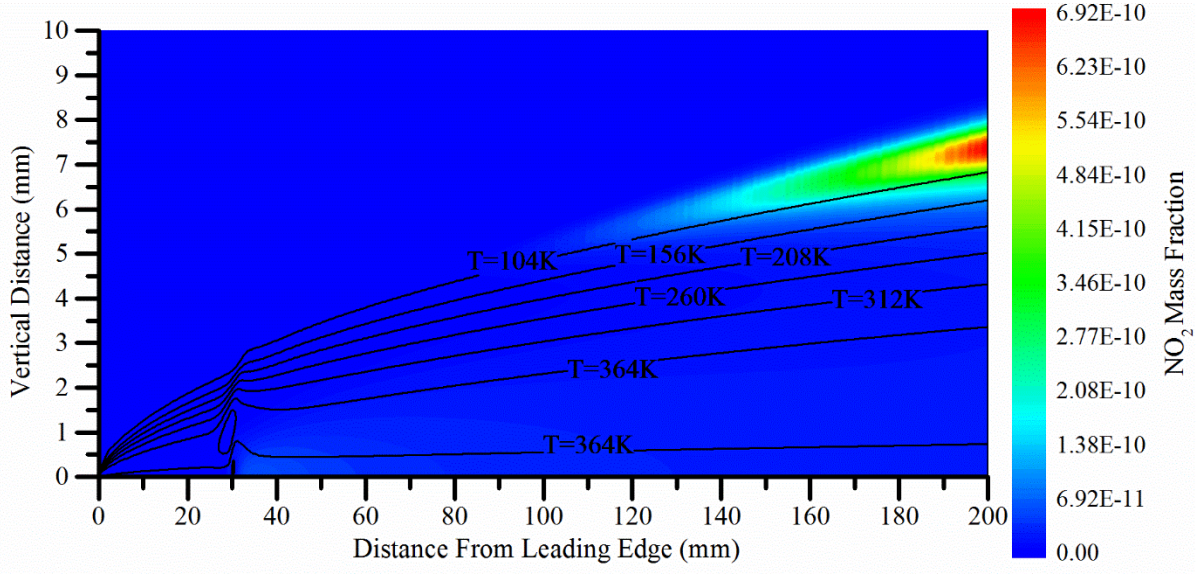

Figure 5.8: Simulated NO_2 distribution P_{stag} = 350 psi; T_{stag} = 1000 K; θ_{plate} = 1° ; Isolines of temperature shown.

Although it was determined that the effects of NO chemical reactions on the flow are negligible at all positive plate angles, some extrapolation of the Olbregt NO reaction rate to approximately 70 K was required. Recall that Olbregt reported reaction rate values over a range of 226 K to 758 K. Therefore, the overall reaction rate was artificially increased by a factor of 10^3 for the θ_{plate} = 1° condition to observe any possible adverse effects on the flow. All of the other flow conditions were kept constant. The location of peak NO formation was found to be the same as in Figure 5.8. Larger amounts of NO_2 were produced at the edge of the boundary layer but NO_2 formation and heat release from the reaction were still found to be negligible. Peak NO concentrations under the 10^3 reaction rate were on the order of 10^{-7}.

At very large reaction rates, the production of NO_2 is limited by the mixing process of NO and O_2. Figure 5.9 shows NO_2 distributions where the reaction rate is increased by a factor of 10^{12}, ensuring that the reaction is complete within the field of view. The peak concentrations of

NO_2 shift away from the edge of the boundary layer (Figure 5.8) to a location just downstream of the seed slot.

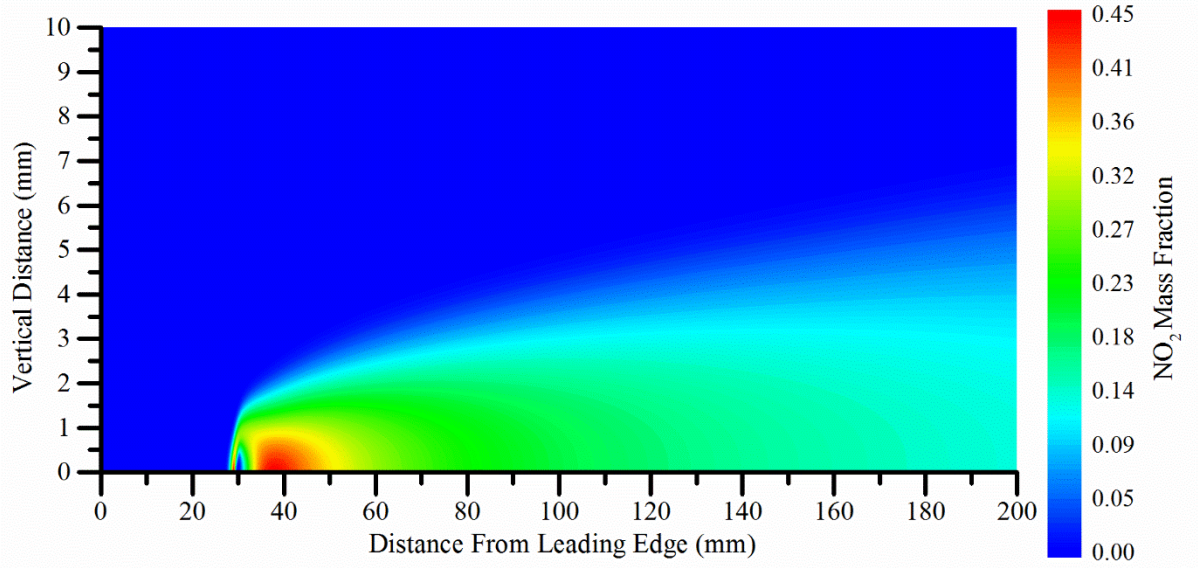

Figure 5.9: Simulated NO_2 distribution; P_{stag} = 350 psi; T_{stag} = 1000 K; θ_{plate} = 1°; Reaction rate increased by a factor of 10^{12};

In this case, the reaction does have adverse effects on the temperature distribution. Temperature deviations upwards of 316 K are observed downstream of the seed slot. This indicates the maximum adverse effects that could occur (assuming an infinitely fast reaction rate) with this level of NO injection. Curiously, high rates of thermal diffusion further downstream allow temperature profiles to return close to their non-reactive case distributions.

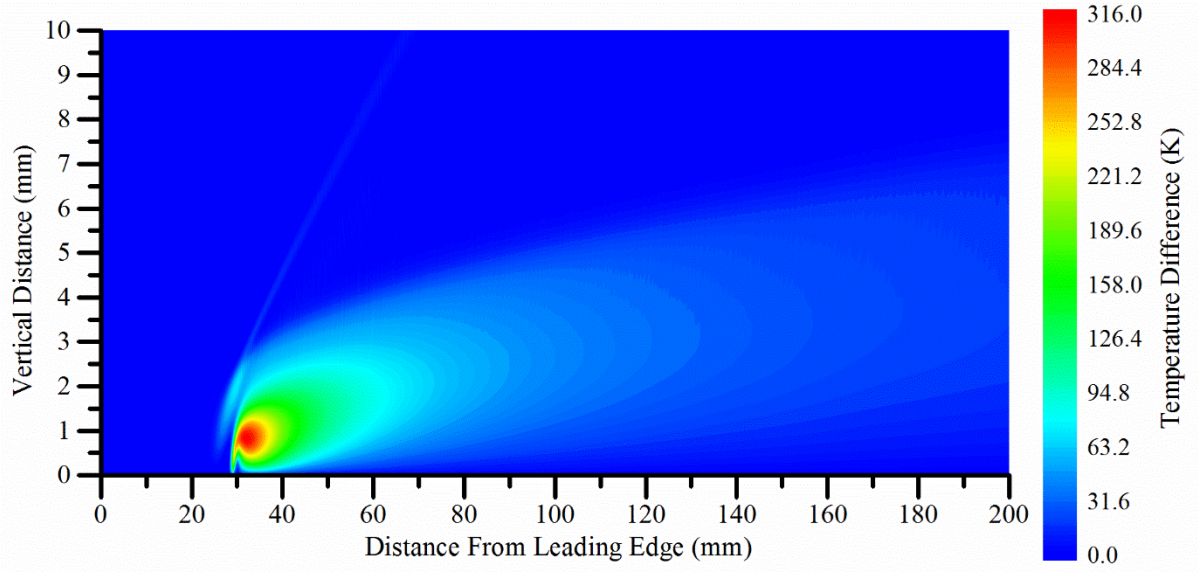

Figure 5.10: Simulated temperature distribution; P_{stag} = 350 psi; T_{stag} = 1000 K; θ_{plate} = 1°; Reaction rate increased by a factor of 10^{12};

5.3 **Chemistry Discussion**

When observing distributions of NO_2 and the reaction rate for the θ_{plate} = 1° case, it is evident that the temperature of the flow governs the reaction rate magnitude. As a result the bulk of the reactions take place near the edge of the boundary layer where the temperature is lowest. For θ_{plate} = 5° the effect of both concentration and temperature are important as reactions occur both near the seed slot and at the edge of the boundary layer. Concentration and temperature have nearly equal effects on the reaction rate at those locations, resulting in NO_2 production of similar magnitudes. Because NO never diffuses beyond the thermal boundary layer in significant quantities, very little reactions occur. The temperature difference due to the heat released by the chemical reaction in the vicinity of the seeding slot was found to be less than 0.5% compared to the nonreactive simulation temperature for both cases.

The analytical model for NO chemistry that assumes a uniform seed gas distribution (Figure 5.4) indicates that the edge conditions for the θ_{plate} = 1° case will result in a static temperature low enough such that chemistry effects will be important. This model assumes that NO escapes beyond the thermal boundary layer and is exposed to the edge conditions. This is however not the case as the seeding simulations indicate that NO does not escape the thermal boundary layer and therefore is not exposed to favorable conditions for NO_2 formation. In addition, the concentration of NO at the edge of the boundary layer is low enough such that only a negligible amount of NO_2 forms. While more NO_2 is produced near the edge of the boundary layer when the wedge AoA is decreased, significant quantities fail to form.

The analytical model that uses a non-uniform seed gas distribution (Figure 5.6) is able to predict the location of the highest concentration of NO_2. As a result, if a reasonable estimate of the distribution of NO is known, the impact of the NO_2 reaction can be estimated using the analytical length scale ratio presented in Eq. (5.17). For significant reactions to occur, the concentration boundary layer would need to be thicker than the thermal boundary layer. However, previous work (C. Johansen & Danehy, 2012) indicates that higher NO seeding rates are not required to achieve sufficient signal-to-noise ratios from the PLIF system in the 31" Mach 10 facility. It is possible that at negative wedge angles, where Prandtl-Meyer expansion would occur, would result in adverse NO chemistry effects. Simulations with artificially amplified reaction rates help to assess the uncertainty involved in extrapolating Olbregt's NO reaction rate to low temperatures (< 226 K). Even with a reaction rate amplified by 10^3, simulations show that the chemistry effects are still negligible. When the reaction rate was amplified to very high levels (10^{12}), the reaction rate was limited by mixing and adverse chemistry effects near the seed slot were observed.

Chapter 6: Conclusions and Recommendations

6.1 Conclusions

The OpenFOAM v2.2.1 based solver rhoCentralReactingFoam was introduced and validated against results from the commercial CFD package ANSYS® Fluent v6.3. Excellent agreement is shown between the two CFD codes and confidence in the rhoCentralReactingFoam solver has been established for future CFD studies. Simulation results for NO seeded at a flow rate of 3 mg/s show excellent agreement with the experimental MTV and pressure tap data.

Localized slip effects were found to have a negligible impact on the 5° AoA wedge simulations performed in previous work. While a significant slip velocity is noticed near the leading edge of the wedge the slip velocity downstream of the gas injection point is small. The leading edge slip was found to slightly alter the shock location but did not significantly alter the shock angle. As a result, the post shock conditions remained the same. These conclusions are further reinforced by the wall pressure distribution, which was found to be unaltered by the slip effects modeled.

The local concentration levels of NO, O_2 and static temperature are the main factors that drive the reaction of NO seeded into a hypersonic boundary layer on a wedge model at positive AoA in NASA Langley's 31-inch Mach 10 facility. Half-life predictions based on uniform NO concentration levels are not reliable in predicting the importance of chemistry effects for locally seeded flows. However, half-life predictions based on simulated NO distributions are able to predict the location and relative magnitude of chemistry effects.

Large magnitudes of the local reaction rate coefficient driven by low static temperatures at the edge of the boundary layer are counter balanced by low concentrations of NO; as a result the reaction rate was found to be negligible for wedge angles greater than and equal to 1° and with

an NO seed rate of 150 sccm or less. While some NO_2 is produced at these conditions, the total amount of heat produced due to chemical reactions is negligible. NO has a very high dispersal rate but is unable to penetrate beyond the thermal boundary layer; resulting in negligible chemical reactions.

Even with the reaction rate amplified by a factor of 10^3, reactions of NO had a negligible impact on the boundary layer flow properties at the conditions simulated. Simulations with artificially high reaction rates indicate that if significant reactions were to occur, they would mainly occur near the wall and seed slot. In this case, the extrapolation of Olbregt's empirical formula below 226 K is unnecessary to predict the reacting flow. At a reaction rate artificially inflated by a factor of 10^{12}, adverse chemistry effects are observed. The bulk of the reactions occur near the seed slot as the reactions become dominated by the mixing of reactants rather than the static temperature.

6.2 **Recommendations for Future Work**

The work described here only assesses the NO chemistry and seeding effects at positive AoA. Further expanding the scope of the work to include negative AoA would provide further benefit. A large number of negative AoA experiments were performed at the wind tunnel facility. Better understanding the effects of NO seeding at negative AoA would allow for the data obtained from those experiments to be used in more meaningful ways. This includes both computational code validation as well as informing future experimental designs. Simulating negative AoA would require a number of modeling considerations. Firstly, rarefied effects start to become more dominant because the Knudsen number increases after the freestream flow passes through the expansion fan that forms in the flow at negative wedge AoA. This means that in addition to slip effects non-equilibrium and non-continuum considerations need to be made when simulating the

flow. With a strong enough expansion, direct simulation Monte Carlo (DSMC) simulations may be required.

In addition to the higher Knudsen number, NO may be exposed to lower temperatures than in the work presented here. In this study the temperature that NO was exposed to was still quite high such that very little extrapolation of the Olbregts reaction rate was required. At negative AoA this may no longer be the case. As a result it is desirable to experimentally determine the reaction rate of NO with NO2 at lower temperatures. This would allow for further confidence in the effect of the NO reaction at negative AoA. Otherwise further extrapolation of the Olbregts reaction rate would be required.

The development and implementation of Computational Fluid Imaging (CFI) models would also be beneficial. A CFI model relates the numerically simulated flow variables to a theoretical PLIF signal and would allow for direct comparisons between simulations and experimental PLIF data. This would be beneficial in that it would allow for validation of the diffusion models used in the CFD simulations. It would also allow for better comparisons to experimental results when more complicated simulations are performed.

With better comparisons to experimental results 3D simulations including the cylindrical trip could be performed. Existing turbulence models could be evaluated; their relative accuracy and ability to predict hypersonic boundary layer transition-to-turbulence determined.

References

Afarin, Y., Tabejamaat, S., & Mardani, A. (2011). Large Eddy Simulation Study of H2/CH4 Flame Structure at MILD Condition. In *Seventh Mediterranean Combustion Symposium*. Sardinia Italy.

Anderson, J. D. (2000). *Hypersonic and high temperature gas dynamics*. American Institute of Aeronautics and Astronautics.

Ankudinov, A. L. (1972). Blowing of a foreign gas in a hypersonic viscous shock layer. *Fluid Dynamics*, *7*(4), 635–640. doi:10.1007/BF01205203

Ashmore, P. G., Burnett, M. G., & Tyler, B. J. (1962). Reaction of nitric oxide and oxygen. *Transactions of the Faraday Society*, *58*, 685–691.

Bansal, A., Feldick, A., & Modest, M. (2012). Simulation of Hypersonic Flow and Radiation over a Mars Reentry Vehicle Using OpenFOAM. In *50th AIAA Aerospace Sciences Meeting including the New Horizons Forum and Aerospace Exposition*. Nashville, TN: American Institute of Aeronautics and Astronautics. doi:10.2514/6.2012-650

Bathel, B., Danehy, P., Inman, J., Alderfer, D., & Berry, S. (2008). PLIF Visualization of Active Control of Hypersonic Boundary Layers Using Blowing. In *26th AIAA Aerodynamic Measurement Technology and Ground Testing Conference*. Seattle, WA: American Institute of Aeronautics and Astronautics. doi:10.2514/6.2008-4266

Bathel, B., Danehy, P., Inman, J., Watkins, A., Jones, S., Lipford, W., … Goyne, C. (2010). Hypersonic Laminar Boundary Layer Velocimetry with Discrete Roughness on a Flat Plate. In *40th Fluid Dynamics Conference and Exhibit*. Chicago, IL: American Institute of Aeronautics and Astronautics. doi:10.2514/6.2010-4998

Bathel, B. F., Danehy, P. M., Inman, J. A., Jones, S. B., Ivey, C. B., & Goyne, C. P. (2010). Multiple velocity profile measurements in hypersonic flows using sequentially-imaged fluorescence tagging. *AIAA Paper*, *1404*.

Battles, B. E., & Hanson, R. K. (1995). Laser-induced fluorescence measurements of NO and OH mole fraction in fuel-lean, high-pressure (1–10 atm) methane flames: Fluorescence modeling and experimental validation. *Journal of Quantitative Spectroscopy and Radiative Transfer*, *54*(3), 521–537. doi:10.1016/0022-4073(95)00020-L

Bogdonoff, S. M. (2012). Preliminary investigations of spiked bodies at hypersonic speeds.

Brodkey, R. S., & Hershey, H. C. (2003). *Transport phenomena: a unified approach* (Vol. 2). Brodkey publishing.

Champigny, P., & Lacau, R. G. (1994). Lateral jet control for tactical missiles. *Tiré À Part-Office National D'études et de Recherches Aerospatiales*.

Chan, S., & Roger, R. (1993). CFD study of the flowfield due to a supersonic jet exiting into a hypersonic stream from a conical surface. II. In *23rd Fluid Dynamics, Plasmadynamics, and Lasers Conference*. American Institute of Aeronautics and Astronautics. doi:10.2514/6.1993-2926

Chapuis, M., Fureby, C., Fedina, E., Alin, N., & Tegnér, J. (2010). Les modeling of combustion applications using OpenFOAM. In *V European Conference on Computational Fluid Dynamics* (pp. 14–17). Libson, Portugul.

Cockburn, B., & Shu, C.-W. (1998). The Runge–Kutta Discontinuous Galerkin Method for Conservation Laws V. *Journal of Computational Physics*, *141*(2), 199–224. doi:10.1006/jcph.1998.5892

Cockrell, C., Barnes, R., Belvin, H., Allmen, J., & Otero, A. (2005). NASA Research Center Contributions to Space Shuttle Return to Flight (SSRTF). In *41st AIAA/ASME/SAE/ASEE Joint Propulsion Conference & Exhibit*. Tucson, Arizona: American Institute of Aeronautics and Astronautics. doi:10.2514/6.2005-3626

Colella, P., & Woodward, P. R. (1984). The Piecewise Parabolic Method (PPM) for gas-dynamical simulations. *Journal of Computational Physics*, *54*(1), 174–201. doi:10.1016/0021-9991(84)90143-8

Combs, C., Clemens, N. T., & Danehy, P. M. (2014). Development of Naphthalene PLIF for Visualizing Ablation Products from a Space Capsule Heat Shield. In *52nd Aerospace Sciences Meeting*. National Harbor, MD: American Institute of Aeronautics and Astronautics. doi:10.2514/6.2014-1152

Danehy, P., Ivey, C., Bathel, B., Inman, J., Jones, S., Jiang, N., … Goodman, K. Z. (2010). Orbiter BLT Flight Experiment Wind Tunnel Simulations: Nearfield Flowfield Imaging and Surface Thermography. In *48th AIAA Aerospace Sciences Meeting Including the New Horizons Forum and Aerospace Exposition*. Orlando, FL: American Institute of Aeronautics and Astronautics. doi:10.2514/6.2010-1571

Danehy, P., Ivey, C., Inman, J., Bathel, B., Jones, S., Jiang, N., … McCrea, A. C. (2010). High-Speed PLIF Imaging of Hypersonic Transition over Discrete Cylindrical Roughness. In *48th AIAA Aerospace Sciences Meeting Including the New Horizons Forum and Aerospace Exposition*. Orlando, FL: American Institute of Aeronautics and Astronautics. doi:10.2514/6.2010-703

Danehy, P. M., Inman, J. A., Brauckmann, G. J., Alderfer, D. W., Jones, S. B., & Patry, D. P. (2009). Visualization of a Capsule Entry Vehicle Reaction-Control System Thruster. *Journal of Spacecraft and Rockets*, *46*(1), 93–102. doi:10.2514/1.34846

Dickmann, D. A., & Lu, F. K. (2006). Jet in supersonic crossflow on a flat plate. *AIAA Paper*, *3451*, 2006.

Dickmann, D. A., & Lu, F. K. (2009). Shock/boundary-layer interaction effects on transverse jets in crossflow over a flat plate. *Journal of Spacecraft and Rockets*, *46*(6), 1132–1141.

Fischer, M. C. (1972). Spreading of a Turbulent Disturbance. *AIAA Journal*, *10*(7), 957–959. doi:10.2514/3.50265

Fox, J. S., P. Houwing, A. F., Danehy, P. M., Gaston, M. J., Mudford, N. R., & Gai, S. L. (2001). Mole-Fraction-Sensitive Imaging of Hypermixing Shear Layers. *Journal of Propulsion and Power*, *17*(2), 284–292. doi:10.2514/2.5775

Fric, T. F., & Roshko, A. (1994). Vortical structure in the wake of a transverse jet. *Journal of Fluid Mechanics*, *279*, 1–47.

Ghaffari, S., Marxen, O., Iaccarino, G., & Shaqfeh, E. S. G. (2010). Numerical simulations of hypersonic boundary-layer instability with wall blowing. *AIAA Paper*, *306*, 2010.

Gharib, H. H. and D. D. and M. (1997). On errors of digital particle image velocimetry. *Measurement Science and Technology*, *8*(12), 1427. Retrieved from http://stacks.iop.org/0957-0233/8/i=12/a=007

Glasson, W. A., & Tuesday, C. S. (1963). The atmospheric thermal oxidation of nitric oxide. *Journal of the American Chemical Society*, *85*(19), 2901–2904.

Greenshields, C. J., Weller, H. G., Gasparini, L., & Reese, J. M. (2010). Implementation of semi-discrete, non-staggered central schemes in a colocated, polyhedral, finite volume framework, for high-speed viscous flows. *International Journal for Numerical Methods in Fluids*, *63*(1), 1–21. doi:10.1002/fld.2069

Greig, J. D., & Hall, P. G. (1966). Infra-red spectrophotometric study of the oxidation of nitric oxide. *Trans. Faraday Soc.*, *62*, 652–658.

Greig, J. D., & Hall, P. G. (1967). Thermal oxidation of nitric oxide at low concentrations. *Trans. Faraday Soc.*, *63*, 655–661.

Gruber, M. R., Nejadt, a. S., Chen, T. H., & Dutton, J. C. (1995). Mixing and Penetration Studies of Sonic Jets in a Mach 2 Freestream. *Journal of Propulsion and Power*, *11*(2), 315–323. doi:10.2514/3.51427

Harten, A., Engquist, B., Osher, S., & Chakravarthy, S. R. (1987). Uniformly high order accurate essentially non-oscillatory schemes, III. *Journal of Computational Physics*, *71*(2), 231–303. doi:10.1016/0021-9991(87)90031-3

Hisatsune, I. C., & Zafonte, L. (1969). Kinetic study of some third-order reactions of nitric oxide. *The Journal of Physical Chemistry, 73*(9), 2980–2989.

Hollis, B. R. (1996). *Real-gas flow properties for NASA Langley Research Center aerothermodynamic facilities complex wind tunnels*. Langley Research Center: National Aeronautics and Space Administration.

Horvath, T. J., Berry, S., Merski, N., Berger, K., Buck, G., Leichty, D., & Schneider, S. (2006). Shuttle Damage/Repair from the Perspective of Hypersonic Boundary Layer Transition - Experimental Results. In *9th AIAA/ASME Joint Thermophysics and Heat Transfer Conference*. San Francisco, CA: American Institute of Aeronautics and Astronautics. doi:10.2514/6.2006-2919

Horvath, T. J., Tomek, D. M., Berger, K. T., Splinter, S. C., Zalameda, J. N., Krasa, P. W., … Tietjen, A. B. (2010). The HYTHIRM Project: Flight Thermography of the Space Shuttle During Hypersonic Re-Entry. In *48th AIAA Aerospace Science Meeting Conference* (Vol. 241). Orlando, FL.

Inman, J. (2007). *Fluorescence imaging study of free and impinging supersonic jets: Jet structure and turbulent transition*. The College of William and Mary.

Inman, J. A., Danehy, P. M., Alderfer, D. W., Buck, G. M., & McCrea, A. C. (2009). Planar Fluorescence Imaging and Three-Dimensional Reconstructions of Capsule Reaction-Control-System Jets. *AIAA Journal*, *47*(4), 803–812. doi:10.2514/1.37116

Jasak, H., Weller, H. G., & Gosman, A. D. (1999). High resolution NVD differencing scheme for arbitrarily unstructured meshes. *International Journal for Numerical Methods in Fluids*, *31*(2), 431–449.

Johansen, C., & Danehy, P. (2012). Numerical investigation of PLIF gas seeding for hypersonic boundary layer flows. In *50th AIAA Aerospace Sciences Meeting including the New Horizons Forum and Aerospace Exposition*. Nashville, TN: American Institute of Aeronautics and Astronautics. doi:10.2514/6.2012-1057

Johansen, C. T., McRae, C. D., Danehy, P. M., Gallo, E. C. A., Cantu, L. M. L., Magnotti, G., … McDaniel, J. C. (2014). OH PLIF visualization of the UVa supersonic combustion experiment: Configuration A. *Journal of Visualization*, *17*(2), 131–141.

John, J. E. A., & Keith, T. G. (2006). *Gas Dynamics*. Pearson Prentice Hall.

John, J., & Keith, T. (1984). *Gas dynamics*. Pearson Education India.

Kennard, E. H. (1938). *Kinetic theory of gases: with an introduction to statistical mechanics*. McGraw-Hill.

Kurganov, A., Noelle, S., & Petrova, G. (2001). Semidiscrete central-upwind schemes for hyperbolic conservation laws and Hamilton--Jacobi equations. *SIAM Journal on Scientific Computing*, *23*(3), 707–740.

Kurganov, A., & Tadmor, E. (2000). New High-Resolution Central Schemes for Nonlinear Conservation Laws and Convection–Diffusion Equations. *Journal of Computational Physics*, *160*(1), 241–282. doi:10.1006/jcph.2000.6459

Laane, J., & Ohlsen, J. R. (1980). Characterization of Nitrogen Oxides by Vibrational Spectroscopy. In *Progress in Inorganic Chemistry* (pp. 465–513). John Wiley & Sons, Inc. doi:10.1002/9780470166284.ch6

Liu, X.-D., Osher, S., & Chan, T. (1994). Weighted Essentially Non-oscillatory Schemes. *Journal of Computational Physics*, *115*(1), 200–212. doi:10.1006/jcph.1994.1187

Matarrese, M. D., Messiter, A. F., & Adamson, T. C. (1991). Control of hypersonic aerodynamic forces with surface blowing. *AIAA Journal*, *29*(12), 2094–2104.

McKenzie, R. L. (1996). Measurement capabilities of planar Doppler velocimetry using pulsed lasers. *Applied Optics*, *35*(6), 948–964.

Medford, T., Danehy, P., Jones, S., Jiang, N., Webster, M., Lempert, W., … Meyer, T. (2011). Stereoscopic Planar Laser-Induced Fluorescence Imaging at 500 kHz. In *49th AIAA Aerospace Sciences Meeting including the New Horizons Forum and Aerospace Exposition*. Orlando, FL: American Institute of Aeronautics and Astronautics. doi:10.2514/6.2011-985

Messiter, a. F., & Matarrese, M. D. (1995). Strip blowing from a wedge at hypersonic speeds. *AIAA Journal*, *33*(5), 843–850. doi:10.2514/3.12372

Micol, J. (1998). Langley Aerothermodynamic Facilities Complex - Enhancements and testing capabilities. In *36th AIAA Aerospace Sciences Meeting and Exhibit*. American Institute of Aeronautics and Astronautics. doi:10.2514/6.1998-147

Morecroft, M. J., & Thomas, J. H. (1967). The reaction between nitric oxide and oxygen. *The Journal of Physical Chemistry*, *71*(5), 1543–1544.

National Institute of Standards and Technology. (2011). NIST-JANAF Thermochemical Tables. Retrieved May 19, 2011, from http://kinetics.nist.gov/janaf/

Nessyahu, H., & Tadmor, E. (1990). Non-oscillatory central differencing for hyperbolic conservation laws. *Journal of Computational Physics*, *87*(2), 408–463. doi:10.1016/0021-9991(90)90260-8

Neufeld, P. D., Janzen, A. R., & Aziz, R. A. (2003). Empirical Equations to Calculate 16 of the Transport Collision Integrals Ω (l, s)* for the Lennard-Jones (12-6) Potential. *The Journal of Chemical Physics*, *57*(3), 1100–1102.

Olbregts, J. (1985). Termolecular reaction of nitrogen monoxide and oxygen: A still unsolved problem. *International Journal of Chemical Kinetics*, *17*(8), 835–848.

Raffel, M., Willert, C. E., Wereley, S. T., & Kompenhans, J. (2007). *Particle Image Velocimetry: A Practical Guide*. Springer. Retrieved from http://books.google.ca/books?id=fdKd50rzfuMC

Schwartz, J. F. M. and J. W. L. and R. J. (2001). Characterization of measurement error sources in Doppler global velocimetry. *Measurement Science and Technology*, *12*(4), 357. Retrieved from http://stacks.iop.org/0957-0233/12/i=4/a=301

Settles, G. S. (2012). *Schlieren and Shadowgraph Techniques: Visualizing Phenomena in Transparent Media*. Springer Berlin Heidelberg. Retrieved from http://books.google.ca/books?id=kF5wkQEACAAJ

Smith, F. T., & Stewartson, K. (1973). Plate-injection into a separated supersonic boundary layer. *Journal of Fluid Mechanics*, *58*(01), 143–159.

Srinivasan, R., & Bowersox, R. (2004). Role of the Barrel Shock as Control Element for Hypersonic Transverse Jet Injection Flows. *AIAA Paper*, *2698*, 2004.

Stemmer, C. (2002). *Flat-plate boundary-layer transition in hypersonic flows*.

Svehla, R. A. (1962). *Estimated viscosities and thermal conductivities of gases at high temperatures*. Lewis Research Center, Cleveland: National Aeronautics and Space Administration. Lewis Research Center, Cleveland.

Tropea, C., Yarin, A. L., & Foss, J. F. (2007). *Springer Handbook of Experimental Fluid Mechanics*. Springer. Retrieved from http://books.google.ca/books?id=y0xDUAdQAlkC

Tsukahara, H., Ishida, T., & Mayumi, M. (1999). Gas-phase oxidation of nitric oxide: chemical kinetics and rate constant. *Nitric Oxide*, *3*(3), 191–198.

Van Leer, B. (1997). Towards the Ultimate Conservative Difference Scheme. *Journal of Computational Physics*, *135*(2), 229–248. doi:10.1006/jcph.1997.5704

Vincenti, W. G., & Kruger, C. H. (1986). *Physical gas dynamics*. Krieger.

Wilke, C. R. (1950). Diffusional properties of multicomponent gases. *Chemical Engineering Progress*, *46*(2), 95–104.